

A survey of the ISM in early-type galaxies*.

I. The ionized gas

F. Macchetto^{1,2}, M. Pastoriza^{1,3}, N. Caon^{1,2}, W.B. Sparks¹, M. Giavalisco⁴, R. Bender⁵ and M. Capaccioli⁶

¹ Space Telescope Science Institute, Baltimore MD, U.S.A.

² Affiliated to the Astrophysics Division, Space Science Department, ESA

³ Instituto de Física, UFRGS, Porto Alegre, Brazil

⁴ The Observatory of the Carnegie Institution of Washington, Pasadena, CA, U.S.A. – Hubble Fellow

⁵ Universitäts-Sternwarte, München, Germany

⁶ Osservatorio Astronomico di Capodimonte, Napoli, Italy

Received December 1, 1995; accepted May 2, 1996

Abstract. — We present results of a CCD optical imaging survey of the ionized gas in 73 luminous elliptical and lenticular galaxies, selected from the RC3 catalog to represent a broad variety of X-ray, radio, infrared and kinematical properties. For each galaxy we have used broad-band R images and narrow-band images centered at the H α and [NII] emission lines to derive the luminosity and distribution of the ionized gas. We found that a large fraction of E (72%) and S0 (85%) galaxies in our sample contain ionized gas. The gas morphology appears to be rather smooth for most galaxies; however $\sim 12\%$ of the sample galaxies show a very extended filamentary structure. According to the morphology and size of the gas distribution, the galaxies have been classified into three broad groups, named small disk (SD), regular extended (RE) and filamentary structure (F). The mean diameter of the emitting region ranges between 1 and 10 kpc; the derived mass of the ionized gas ranges between 10^3 and 10^5 solar masses. A significant correlation between H α + [NII] and X-ray luminosities is found for those galaxies (27% of the sample) for which we have detected ionized gas and are also listed as X-ray sources. However, there are relatively strong X-ray emitting galaxies for which we have not detected H α + [NII] emission and objects which show emission-lines but are not listed either in the EINSTEIN or in the ROSAT databases. The distribution of datapoint and upper limits in this diagram suggests that galaxies with warm gas are also X-ray emitters, while there are X-ray emitters without measurable H α + [NII] emission. Similar characteristics are present in the correlation between the infrared luminosity in the 12 μ m band and $L_{\text{H}\alpha+\text{[NII]}}$; correlations with other infrared wavelengths are weaker. A strong correlation was also found between the H α + [NII] luminosity and the luminosity in the B band inside the region occupied by the line-emitting gas. We use these correlations to discuss the possible mechanisms responsible for the gas ionization and excitation, analyzing in particular the role of the post-AGB stars and the thermal conduction from the X-ray halo in providing the necessary source of ionization.

Key words: galaxies: elliptical and lenticular — galaxies: ISM — galaxies: structure

1. Introduction

Optical surveys have shown that a large percentage of early-type galaxies contain extended dust lanes, patches or a central disk-like dust structure (Sadler & Gerhardt 1985; Sparks et al. 1985; Macchetto & Sparks 1992; Goudfrooij et al. 1994, hereinafter GHJN). In addition to the dust, warm (10^4 K) ionized gas is present in a high fraction of ellipticals, of the order of 50%, as shown by spectroscopic and/or imaging surveys. The amount of ionized gas is of

the order of 10^3 – 10^4 solar masses (Caldwell 1984; Phillips et al. 1986, hereinafter PJDSB; GHJN). Although relatively small in mass, the contribution to the energy budget of the galaxy can be very large. The optical line-emission can dominate, at least locally, the energy loss from X-rays (Sparks et al. 1989, hereinafter SMG) and therefore it has to be understood in order to derive a correct description for the energetics of the interstellar medium in these galaxies.

The nature, the origin and the future evolution of the gas and dust in elliptical galaxies is still a highly controversial subject. A first scenario is one in which the ISM is a normal, quiescent component of these early-type

Send offprint requests to: F. Macchetto

*Based on observations collected at the European Southern Observatory, within the ESO Key-Programme 1-004-43K

galaxies. An alternative scenario is that in which clouds of cold gas and dust have been accreted in merger events and heated by thermal conduction from the X-ray emitting plasma (SMG; Kim 1989). Finally there is the cooling-flow scenario in which the stellar mass-loss, heated at high temperatures (10^6 – 10^7 K) by supernovae explosions during the galaxy formation, cools and condenses into filaments (see Fabian 1994, for a review).

In addition to the origin, neither the excitation mechanism nor the ultimate fate of this gas are well established. Photoionization by hot young stars (Kim 1989; Shields 1991, hereinafter S91), by hot old stars (di Serego Alighieri et al. 1990; Binette et al. 1994, hereinafter BMSB) or radiation originating in an active nucleus (Fosbury et al. 1982) are among the competing theories, along with shocks (Heckman et al. 1989). Ionization linked with X-ray emitting gas is another alternative proposed to explain the observed emission lines and their excitation character (SMG; Donahue & Voit 1991).

In order to study the properties of the interstellar medium in early-type galaxies and elucidate its origin, we have carried out an extensive program of imaging and spectroscopic observations of a large sample of bright elliptical and lenticular galaxies. The galaxies in our sample have been selected so as to span a wide range of optical, X-ray, radio, infrared and kinematical properties. The observations have been aimed at reaching fainter limiting-flux levels than in previous studies, in order to provide a more complete and extensive mapping of the ionized-gas distribution, especially of those faint filamentary structures extending far out from the galaxy nucleus.

In this paper we present results of CCD observations for 39 ellipticals and 34 lenticular galaxies. For each galaxy we have obtained the total luminosity, morphology and extension of the ionized gas. We have explored the correlations between the ionized gas luminosity and other global properties of the galaxies, e.g. X-ray, IR and radio emission, available in the literature and electronic databases. Although a thorough and complete statistical analysis of these correlations is outside the scope of the present paper, the results shown here provide valuable information on the physics of the ionized gas. In particular, we discuss the viability of UV photons emitted by post-AGB stars and the conductive heating by hot electrons associated with an X-ray emitting coronal halo as the dominant ionizing sources.

This paper is structured as follows: in Sect. 2 we present the galaxy sample, in Sect. 3 we describe the observations and data reduction. The morphology of the ionized gas is presented in Sect. 4. In Sect. 5 we analyze the correlations between the $H\alpha$ + $[NII]$ luminosities and X-ray, IR and radio fluxes. The possible mechanisms for the ionization and excitation of the gas are briefly discussed in Sect. 6. Concluding remarks are given in Sect. 7.

2. The sample

The early-type galaxies studied in this paper are all luminous galaxies ($B_T \lesssim 13.0$ mag), with morphological type E or S0 (including S0/Sa) according to both the Third Reference Catalogue of Bright Galaxies (RC3; de Vaucouleurs et al. 1991) and the Revised Shapley-Ames Catalog of Bright Galaxies (RSA; Sandage & Tammann 1987), selected to span the entire variety of morphological types and isophotal shapes from E0 through S0/Sa, to provide a fair interval of optical luminosity, and to include both radio-loud and radio-quiet, X-ray emitters and non-emitters.

The galaxies in our sample are listed in Table 1, along with their morphological types, magnitudes, and extinction in the blue band taken from the RC3 catalogue. The distances have been derived from the “220 model” for the Virgo infall of Kraan-Korteweg (1986), assuming a Virgo Cluster distance of 21.3 Mpc, which corresponds to a Hubble constant $H_0 = 55 \text{ km s}^{-1} \text{ Mpc}^{-1}$ (see Jerjen & Tammann 1993). For galaxies belonging to a group or cluster, the same distance has been taken, following Davies et al. (1987). For those galaxies not present in Kraan-Korteweg’s compilation, the distance has been derived from the redshift reduced to the reference frame defined by the cosmic microwave background (from RC3).

The luminosity distribution for the galaxy sample is presented in Fig. 1: the absolute blue magnitudes of our galaxies range between -19.0 and -23.5 , with a maximum at $M_B = -21.5$.

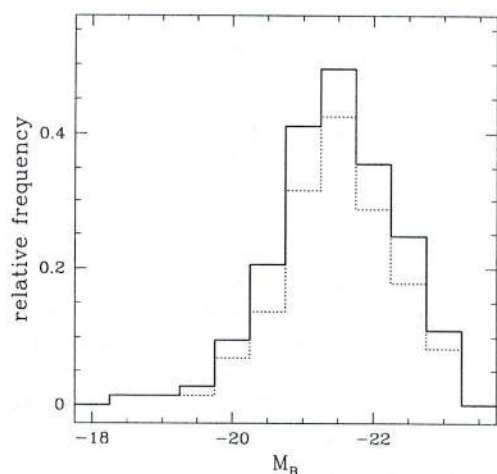


Fig. 1. The luminosity function of our galaxy sample. The dashed histogram refers to those galaxies with positive $H\alpha$ + $[NII]$ detection

Table 1. The galaxy sample

Ident	RA (2000)	DEC	type	B_T^0	A_B
NGC 524	01 24 47.8	+09 32 21	S0/Sa	11.17	0.03
NGC 533	01 25 31.5	+01 45 35	E3	12.22	0.06
NGC 584	01 31 20.9	-06 52 06	S0	11.21	0.14
NGC 596	01 32 52.1	-07 01 57	E0/S0	11.66	0.11
NGC 636	01 39 06.6	-07 30 47	E1	12.22	0.13
NGC 720	01 53 00.4	-13 44 21	E5	11.13	0.00
NGC 741	01 56 20.9	+05 37 44	E0	12.07	0.14
NGC 821	02 08 21.1	+10 59 44	E6	11.72	0.17
NGC 1172	03 01 36.1	-14 50 13	S0	12.56	0.11
NGC 1399	03 38 29.0	-35 26 58	E1	10.44	0.00
NGC 1400	03 39 31.3	-18 41 19	S0	11.89	0.14
NGC 1407	03 40 12.4	-18 34 52	E0/S0	10.71	0.17
NGC 1453	03 46 27.3	-03 58 10	E0	12.26	0.25
NGC 1600	04 31 39.9	-05 05 16	E4	11.83	0.08
NGC 2865	09 23 30.8	-23 09 48	E4	12.18	0.29
NGC 3115	10 05 14.1	-07 43 07	S0	9.74	0.10
NGC 3268	10 30 00.6	-35 19 30	E2	12.26	0.28
NGC 3311	10 36 43.3	-27 31 41	S0	12.22	0.18
NGC 3379	10 47 49.9	+12 34 57	E0	10.18	0.05
NGC 3489	11 00 18.2	+13 54 08	S0/Sa	11.15	0.02
NGC 3607	11 16 54.1	+18 03 12	S0	10.79	0.00
NGC 4105	12 06 40.7	-29 45 42	S0	11.34	0.25
NGC 4472	12 29 46.5	+07 59 58	E1/S0	9.33	0.00
NGC 4473	12 29 48.8	+13 25 49	E5	11.03	0.07
NGC 4486	12 30 49.7	+12 23 24	E0	9.49	0.10
NGC 4552	12 35 39.9	+12 33 25	S0	10.57	0.15
NGC 4636	12 42 49.8	+02 41 17	E0/S0	10.43	0.05
NGC 4782	12 54 35.8	-12 34 06	E0	12.56	0.07
NGC 4936	13 04 16.4	-30 31 29	E2	11.36	0.36
NGC 5044	13 15 24.0	-16 23 09	E0	11.67	0.12
NGC 5077	13 19 31.7	-12 39 26	S0	12.21	0.08
NGC 5090	13 21 13.5	-43 42 18	E2	11.97	0.52
NGC 5102	13 21 57.8	-36 37 47	S0	9.99	0.22
NGC 5419	14 03 38.6	-33 58 41	S0	11.44	0.25
NGC 5532	14 16 52.8	+10 48 24	S0	12.77	0.00
NGC 5812	15 00 55.8	-07 27 29	E0	11.83	0.32
NGC 5813	15 01 11.2	+01 42 08	E1	11.42	0.16
NGC 5831	15 04 07.2	+01 13 15	E4	12.31	0.15
NGC 5846	15 06 29.4	+01 36 25	S0	10.91	0.15
NGC 5864	15 09 33.8	+03 03 11	SB0	12.63	0.11
NGC 5898	15 18 13.3	-24 05 49	S0	11.92	0.51
NGC 5903	15 18 36.3	-24 04 06	E3/S0	11.74	0.51

3. Observations and data reduction

3.1. Observations

The observations were carried out during several runs at the European Southern Observatory (La Silla, Chile) with the 3.6 m and the NTT telescopes. CCD images were acquired both through a broad-band R filter matching the Cousins standard band and through a narrow-band filter centered on the $H\alpha$ + $[NII]$ emission lines. The instruments and setups used in the various observing runs are shown in Table 2; the filters' specifications are shown in Table 3. The exposure times were selected in order to achieve good signal-to-noise ratios in each of the two bands and to reach faint surface brightness levels. Two or more frames

with each filter were taken for each galaxy to allow for easy removal of cosmic ray events. Typically, $H\alpha$ frames were exposed 25–45 min, while R images have exposure times in the range 30 s–3 min. The images have been processed with the Image Reduction and Analysis Facility (IRAF), using the standard techniques for bias and dark-current subtraction, division by normalized twilight flat-fields, and interpolation over bad columns and/or pixels. The sky level was determined by calculating the average intensity in blank regions in the frames, and subsequently subtracted out. While this value may be somewhat affected by contamination by the light from the galaxy, the residual in the sky background subtraction cancel out in the subtraction of the rescaled continuum image from the narrow-band image (see below). The residual cosmic rays

Table 1. continued

Ident	RA (2000)	DEC	type	B_T^0	A_B
NGC 5920	15 21 51.8	+07 42 32	S0	14.37	0.08
NGC 6034	16 03 32.4	+17 11 53	E?	14.38	0.05
NGC 6305	17 18 00.5	-59 10 18	E/S0	12.58	0.54
NGC 6407	17 18 00.5	-59 10 18	E	12.43	0.37
NGC 6483	17 59 29.8	-63 40 07	E	12.63	0.33
NGC 6721	19 00 50.5	-57 45 28	E1	12.68	0.28
NGC 6758	19 13 52.3	-56 18 33	E2	12.31	0.22
NGC 6776	19 25 19.4	-63 51 41	E1 pec	12.71	0.20
NGC 6851	20 03 33.6	-48 17 02	E4	12.51	0.17
NGC 6861	20 07 19.2	-48 22 12	S0	11.92	0.15
NGC 6868	20 09 53.8	-48 22 45	E3/S0	11.49	0.15
NGC 6875	20 13 12.4	-46 09 38	S0	12.78	0.00
NGC 6876	20 18 20.3	-70 51 28	E3	11.83	0.17
NGC 6909	20 27 38.7	-47 01 34	E5	12.51	0.07
NGC 6936	20 35 56.6	-25 16 46	SA0	13.52	0.19
NGC 6964	20 47 24.0	+00 18 02	E pec	13.38	0.39
NGC 7014	21 07 52.6	-47 10 40	E5	13.02	0.07
NGC 7029	21 11 52.4	-49 16 58	S0	12.42	0.00
NGC 7041	21 16 32.6	-48 21 51	S0/E7	12.19	0.07
NGC 7049	21 19 00.3	-48 33 50	S0/Sa	11.57	0.03
NGC 7192	22 06 50.0	-64 18 57	S0	12.23	0.00
NGC 7196	22 05 54.7	-50 07 11	E3/S0	12.35	0.00
NGC 7562	23 15 57.4	+06 41 15	E2	12.37	0.23
NGC 7619	23 20 14.7	+08 12 23	E3	11.93	0.17
NGC 7626	23 20 42.4	+08 13 02	E1	12.06	0.17
NGC 7796	23 58 59.8	-55 27 24	E1	12.39	0.00
IC 1459	22 57 09.5	-36 27 37	E	10.83	0.04
IC 4296	13 36 38.9	-33 57 59	E0	11.42	0.13
IC 4797	18 56 29.3	-54 18 22	E pec	11.85	0.31
IC 4889	19 45 15.9	-54 20 37	S0	11.91	0.19
IC 5105	21 24 22.2	-40 32 11	E5	12.42	0.07

Notes to the table:

Coordinates, blue apparent magnitudes B_T^0 , corrected for galactic and internal absorption and for redshift, and galactic absorption in the B -band A_B have been taken from RC3.

The morphological type is as listed in the RSA catalog.

present in the frames were identified as those pixels whose values are larger than the local mean value by more than 5 sigma, and replaced by a median value calculated over the nearest 5×5 pixels.

3.2. Emission-line images generation

Several data reduction steps have to be performed before generating emission-line intensity images. The first step is to align, for each galaxy, the broad-band and narrow-band images to an accuracy of a few hundredths of a pixel. This was achieved by measuring the centers of the common stars in the images, after fitting gaussians to the stars profiles, and then registering and convolving the image(s) with the best seeing to match the seeing of the other image. This minimizes the degradation of the resolution in our data. For each galaxy, a final emission-line and a final R image were thus produced, summing the images in each set. In turn, these two final images were aligned and brought to the same resolution.

The most important step in the data reduction process, as well as the principal source of error, is the determination of the intensity scale factor that has to be applied to the final R image in order to match the stellar continuum in the final narrow-band image, so as to give the pure emission $H\alpha + [NII]$ image once it is subtracted out.

The final R scaled image was obtained through the following procedure. Ellipses were fitted to the isophotes for both the combined R and emission-line images using the task “ellipse” of the Space Telescope Science Data Analysis System (STSDAS), which produces a table containing the isophotal parameters. These data allow us to plot, for the isophotes with the same major semidiameter a , the corresponding mean count levels N_R versus N_{NB} . A least square fit was made to the outer isophotes, in the radial range where the stellar continuum light dominates, avoiding the inner regions where the signal from the ionized gas is expected to be significant. The slope of the fit gives the scale factor ε between the continuum flux in the R band and that in the emission-line band, while the

Table 2. Observational set-ups

Run	Instrument & detector pixel size & FOV		ESO filters		Galaxies
			H α + $[\text{NII}]$	R	
Oct 3–6, 1989	3.6m+EFOSC 0''337	CCD#8 3'7 \times 5'8	388, 389	554	NGC 584, NGC 720, NGC 1172, NGC 1399, NGC 1407, NGC 1453, NGC 6868, NGC 6876, NGC 7562, NGC 7626
Mar 30–Apr 1 1990	NTT+EFOSC2 0''257	CCD#5 1'4 \times 2'2	388, 436, 438, 439, 441	585	NGC 2865, NGC 3268, NGC 3311, NGC 3379, NGC 4105, NGC 4472, NGC 4473, NGC 4486, NGC 4552, NGC 4782, NGC 5044, NGC 5077, NGC 5090, NGC 5102, NGC 5812, NGC 5813, NGC 5898, NGC 5903, NGC 5920, IC 4296
Aug 17–21, 1990	NTT+EFOSC2 0''300 (binned)	CCD#17 2'7 \times 2'6	388, 438, 439	585	NGC 524, NGC 596, NGC 636, NGC 741, NGC 821, NGC 1400, NGC 5846, NGC 6034, NGC 6305, NGC 6407, NGC 6483, NGC 6758, NGC 6875, NGC 6909, NGC 7014, NGC 7041, NGC 7049, NGC 7192, NGC 7619, NGC 7796, IC 4797, IC 4889, IC 5105
May 12–16, 1991	NTT+EMMI 0''350	CCD#24 9'2 \times 8'6	595, 596, 597, 598	608	NGC 3115, NGC 3489, NGC 3607, NGC 4636, NGC 4936, NGC 5419, NGC 5532, NGC 6776, NGC 7029
Aug 21–24, 1993	NTT+EMMI 0''340	CCD#34 9'2 \times 8'6	595, 597, 598, 653	608	NGC 533, NGC 1600, NGC 5831, NGC 5864, NGC 6721, NGC 6851, NGC 6861, NGC 6936, NGC 6964, NGC 7196, IC 1459

intercept k , usually close to 0, depends on the residuals in the sky background in the two images.

$$N_R = \varepsilon \times N_{\text{NB}} + k \quad (1)$$

In some cases, a visual inspection of the continuum-subtracted image made it necessary to iterate the fit adjusting the radial range so as to completely exclude from the fit regions affected by line emission. The formal uncertainty in the scale factor is usually less than 1%; for a few cases, especially for galaxies with extended emission, we found uncertainties as large as 2–3%.

There were a few cases, for instance IC 4889 and NGC 5044, where the scale factor could not be accurately determined using the method described above, because the region of the galaxy devoid of line emission was too small to give reliable results. We determined the scale factor ε by measuring the mean values inside boxes of 10×10 pixels whose location was carefully chosen to avoid the presence of ionized gas, and then performing a least square fit between the mean values in the R and H α + $[\text{NII}]$ images.

The accuracy of the scale factor was checked, for all galaxies, on the continuum subtracted image, where the resulting values should be zero in the outer regions where there is no presence of ionized-gas emission.

In order to compute the total counts $N(\text{H}\alpha + [\text{NII}])$ for the H α + $[\text{NII}]$ emission, we set to zero, in the pure emission-line images, all the pixel values under a given threshold (typically 1 to 2 rms of the background level). This allows to better define the emitting region and to reduce the effect of possible inhomogeneities in the background when integrating the flux over a large area. This threshold was adjusted to the specific photometric quality of each image and to the characteristic of the emitting region (for instance, a low value was selected if required to avoid to clip-out the faint and diffuse emission seen in some of our objects).

We checked the consistency of this procedure by comparing the resulting $N(\text{H}\alpha + [\text{NII}])$ values obtained with different threshold levels. They change by less than 5% for thresholds varying from 0 (i.e. no threshold applied) to 2 sigma for those galaxies showing a concentrated, disk-like emission. However, for galaxies with extended and diffuse emission, this value can change by as much as 20–25%, indicating that a high value for the threshold is not appropriate since it eliminates areas with true emission. In general, these threshold levels range from 0.1 to 1.0 10^{-16} erg s $^{-1}$ cm $^{-2}$ arcsec $^{-2}$; individual threshold levels for each object are given in Figs. 9.

The relative error on the computed total H α + $[\text{NII}]$ luminosity associated with the uncertainty on ε depends on

Table 3. Filter specifications

Filter number ESO #	λ_{cent} (Å)	FWHM (Å)	Peak trans. (%)
388	6597	77	86
389	6646	80	84
436	6560	63	70
438	6632	69	67
439	6686	82	58
441	6832	74	66
595	6587	73	54
596	6547	73	53
597	6620	66	63
598	6665	66	59
653	6579	32	55
554	6438	1666	86
585	6431	1654	87
608	6390	1498	85

the equivalent width of the ionized-gas emission, which may be varying across the gas distribution. Galaxies with faint and diffuse emission, having on average a small equivalent width, are those most affected, while galaxies with a strong and concentrated emission are the least sensitive. Further possible sources of error are the sky-subtraction, photon noise, residual spatial variations after flat-fielding, an inaccurate alignment and PSF matching between the two images, the selection of the threshold, the uncertainty on the zero-point calibration and the unknown line ratios (see below). Since an estimate of the total uncertainty on our final emission-line images that takes properly into account all of these potential source of errors would be quite impractical, we adopted a more heuristic and straightforward approach. We compared the results obtained for those few objects observed in two different observing runs (and thus with two different telescope, filter and detector combinations), or for the same set of images reduced independently by two different authors. The typical difference turned out to be of the order of 10–15%, and occasionally somewhat larger for galaxies with faint extended emission. As we shall discuss later, comparison with previous published studies shows a much larger discrepancy.

We should note that, since the H α and [NII] lines fall inside the R -passband, the subtraction of the rescaled R image also implies a partial subtraction of the H α + [NII] emission. The magnitude of this effect is equal to the ratios of the effective widths of the narrow-band and R filters used in the observations (we adopted an average value 0.04 for all filter combinations); the final counts have been corrected accordingly.

It also has to be noted that, because we match the seeing profile of the narrow-band and broad-band images to the lowest resolution achieved, we are insensitive to changes in the PSF. Furthermore, the matching technique and image normalization and calibration procedure make the final results insensitive to moderate changes in atmospheric transmission. The main effect of *large* changes in atmospheric transmission would be an increase in the value of the threshold and therefore a small reduction in the detection of the faintest emission features. The resolution of the final emission-line images is given in the captions to Figs. 9.

3.3. Flux calibration

The measured H α + [NII] counts have been converted into an absolute flux scale using the following procedure.

First we calibrated the continuum emission by measuring in our R images a set of integrated counts inside centered circular apertures matching those listed in the photoelectric photometry catalogs (de Vaucouleurs & Longo 1987; Poulain & Nieto 1994). Using these data we determined the zero point R_0 by a least-square fit to the equation:

$$R(< r) = R_0 - 2.5 \log N(< r) \quad (2)$$

where $N(< r)$ is the number of counts inside a centered circular aperture of radius r , and $R(< r)$ is the corresponding magnitude.

The flux corresponding to a star of $R = 0$ mag is $f_0 = 2.13 \cdot 10^{-9} \text{ erg s}^{-1} \text{ cm}^{-2} \text{ Å}^{-1}$ at 6500 Å (in the Cousins photometric system). This factor has been computed with the task “calcphot” in IRAF/STSDAS, using the transmission curves of our R filters and the spectral energy distribution of Vega. The conversion from counts to flux for the CCD R image is thus given by:

$$F_R = N_R \cdot 2.13 \cdot 10^{-9} \cdot 10^{-0.4R_0} \text{ erg s}^{-1} \text{ cm}^{-2} \text{ Å}^{-1} \quad (3)$$

Replacing N_R in this equation by (1) we can derive the flux conversion for the continuum in the narrow-band image

$$F_{\text{NB}} = \varepsilon N_{\text{NB}} \cdot 2.13 \cdot 10^{-9} \cdot 10^{-0.4R_0} \quad (4)$$

The flux of a line emission at wavelength λ_i , where the filter has transmission S_i , is then given by:

$$F_i = \varepsilon N(\text{H}\alpha + [\text{NII}]) \cdot 2.13 \cdot 10^{-9} \cdot 10^{-0.4R_0} \cdot W \cdot (\langle \lambda \rangle / \lambda_i) \cdot (S_{\text{peak}} / S_i) \text{ erg s}^{-1} \text{ cm}^{-2} \quad (5)$$

where W is the effective width of the narrow filter (i.e. the width of a rectangular filter with the same area and constant S_{peak} throughput, S_{peak} being the peak wavelength of the filter), and $\langle \lambda \rangle$ is the average wavelength of the filter. Actually, since both the H α and the [NII] lines fall within the narrow-filter transmission curve, S_i

has been computed as the average of the filter transmissions in correspondence of the three lines, weighted by their intensity. For those galaxies with no measurement of the $[\text{NII}]/\text{H}\alpha$ ratios, we assumed $[\text{NII}]\lambda 6584/\text{H}\alpha = 1.38$ (see Sect. 4.2). Since narrow-band filters have boxy transmission functions, alternate choices for the lines ratios are likely to modify the computed flux by less than 10%.

The $\text{H}\alpha + [\text{NII}]$ fluxes were then corrected for galactic extinction assuming $A_{6563}/E(B - V) = 2.48$, and finally for redshift. No attempt was made to correct fluxes for internal extinction by dust. The luminosities $L_{\text{H}\alpha + [\text{NII}]}$ have been calculated using the distances derived from the Kraan-Korteweg (1986) Virgo infall model.

The observed fluxes, luminosities, linear diameters and morphology of the emitting regions are listed in Table 4. Also listed are the $\text{H}\alpha/[\text{NII}]$ ratios and the derived mass of the ionized gas (see Sect. 4.2).

The estimate of an upper limit for the flux is made difficult by the fact that the detection of a given amount of $\text{H}\alpha + [\text{NII}]$ emission depends on several factors such as its morphological distribution, the brightness of the continuum background, the photometric quality of the images, etc. Thus, we have calculated the upper limits in the following empirical way. Guided by the characteristics of the emission in galaxies with the faintest $\text{H}\alpha + [\text{NII}]$ fluxes, we assumed that a positive detection requires that the pixel values in the pure $\text{H}\alpha + [\text{NII}]$ image be significantly higher than the limiting flux in at least an area of about 100 pixels ($\sim 10 \text{ arcsec}^2$). We therefore set the upper limits to be twice the limiting flux (determined from the noise measured in the pure $\text{H}\alpha + [\text{NII}]$ images) integrated over an area of one hundred pixels.

Our measurements are of course insensitive to diffuse gas distributed as the underlying stellar population, since its contribution would be absorbed in the scaling factor between narrow- and broad-band images. However, previous comparisons of the scaling factors with the theoretical expected values, computed from the filters efficiencies (TdSA), and with spectrophotometric measurements (GHJN), show that such component, if at all present, is very small.

3.4. Comparison with previous measurements

Some of the galaxies in our sample have previously measured fluxes (Trinchieri & di Serego Alighieri 1991, hereinafter TdSA; S91; Hansen et al. 1991; Buson et al. 1993; GHJN; McMillan et al. 1994; Singh et al. 1995). Our results are compared with these previous determinations in Fig. 2; where available, the same aperture used by other observers has been used to measure our fluxes. S91 lists the integrated $\text{H}\alpha + [\text{NII}]$ flux in different apertures ranging from 0.5 to 2 kpc in radius; for this comparison, we have chosen either the largest aperture with measured flux, or the smallest aperture available for those objects having only upper limits. This figure shows reasonable

agreement (differences equal or less than a factor of 3) for most galaxies, with the exception of a few discrepant objects. The agreement seems to be better with TdSA and Buson et al. (1993) data than with GHJN and Singh et al. (1995). The magnitude of the scatter in $\text{H}\alpha + [\text{NII}]$ fluxes we find here is in line with the results from previous comparisons, see for instance Table 7 in GHJN and Fig. 7 in Buson et al. (1993). The most discrepant objects in Fig. 2 are: IC 1459, for which GHJN measure a flux much higher than our value and those published by S91 and Buson et al. (1993); NGC 720, where we find significant emission, in disagreement with both GHJN and S91, who did not detect any emission; NGC 1407, which has been “marginally detected” by GHJN; NGC 3607, for which Singh et al. (1995) measured a flux about five times larger than our value; NGC 1399, where there is a discrepancy of more than an order of magnitude between Singh et al. (1995) and GHJN. Among the objects in our sample not detected in $\text{H}\alpha + [\text{NII}]$, the only one with previous measurements is IC 4296, for which both GHJN and S91 find an emission concentrated in the inner $5''$. Unfortunately, our images (both R and narrow-band) are saturated in the galaxy center, which therefore has prevented the detection of emission. The mean of the residuals (excluding upper limits) plotted in Fig. 2 is -0.03 , with a rms of 0.40. Part of the scatter in the figure may possibly be due to systematic differences in the computation and calibration of previous data, and to the different flux thresholds in the various studies, which is very critical for galaxies with extended emission.

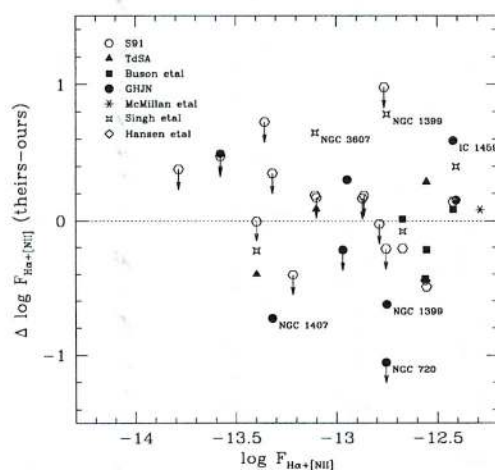


Fig. 2. Comparison of our $\text{H}\alpha + [\text{NII}]$ fluxes with the literature data

Table 4. Data on our sample galaxies

Ident.	Type	Dist. (Mpc)	M_B	$f_{\text{H}\alpha+\text{[NII]}}$ $10^{-14} \text{ erg s}^{-1} \text{ cm}^{-2}$	$L_{\text{H}\alpha+\text{[NII]}}$ $10^{39} \text{ erg s}^{-1}$	$[\text{NII}]\lambda 6584/\text{H}\alpha$	$\log M_{\text{HII}}$	D_{maj} (kpc)	D_{min}	Morph.
NGC 524	S0/Sa	44.1	-22.05	4.41	10.3	—	3.92	8.6	8.4	RE
NGC 533	E3	96.7	-22.71	7.14	79.9	—	4.82	15.4	6.1	F
NGC 584	S0	33.2	-21.40	13.71	18.1	—	4.17	4.8	3.8	RE
NGC 596	E0/S0	33.2	-20.95	< 0.03	< 0.1	—	—	—	—	—
NGC 636	E1	33.2	-20.39	3.64	4.8	—	3.60	1.2	0.6	SD
NGC 720	E5	30.0	-21.26	17.66	19.1	—	4.19	5.0	2.5	SD
NGC 741	E0	99.3	-22.91	2.45	28.9	—	4.38	11.3	5.4	RE
NGC 821	E6	30.0	-20.67	< 0.05	< 0.1	—	—	—	—	—
NGC 1172	S0	27.1	-19.60	2.72	2.4	—	3.29	4.6	2.0	F
NGC 1399	E1	26.2	-21.65	17.82	14.6	—	4.08	3.0	2.4	SD
NGC 1400	S0	29.2	-20.44	< 0.09	< 0.1	—	—	—	—	—
NGC 1407	E0/S0	29.2	-21.62	4.82	4.9	—	3.60	3.5	2.9	SD
NGC 1453	E0	69.9	-21.96	8.76	51.2	—	4.62	18.1	10.7	RE
NGC 1600	E4	83.9	-22.79	4.01	33.9	—	4.44	11.7	4.9	F
NGC 2865	E4	48.4	-21.24	< 0.15	< 0.5	—	—	—	—	—
NGC 3115	S0	8.7	-19.97	< 0.22	< 0.1	1.0	—	—	—	—
NGC 3268	E2	57.5	-21.54	0.36	1.4	—	3.16	1.9	1.9	SD
NGC 3311	S0	63.9	-21.81	0.53	2.6	—	3.33	1.5	1.5	SD
NGC 3379	E0	14.5	-20.62	10.08	2.7	—	3.35	1.4	1.0	SD
NGC 3489	S0/Sa	9.2	-18.66	51.89	5.2	—	3.63	1.3	0.8	SD
NGC 3607	S0	14.7	-20.05	7.83	2.0	—	3.22	1.6	0.9	SD
NGC 4105	S0	34.9	-21.38	13.47	19.7	—	4.21	8.4	5.0	RE
NGC 4472	E1/S0	21.3	-22.31	17.30	9.4	—	3.89	3.0	1.3	SD
NGC 4473	E5	21.3	-20.61	2.65	1.4	—	3.07	1.2	0.9	SD
NGC 4486	E0	21.3	-22.15	188.32	102.2	—	4.92	6.8	5.2	F
NGC 4552	S0	21.3	-21.07	7.96	4.3	1.3	3.57	1.6	1.1	SD
NGC 4636	E0/S0	21.3	-21.21	21.37	11.6	—	3.98	3.1	2.3	SD
NGC 4782	E0	82.6	-22.03	3.61	29.5	—	4.38	4.1	2.6	SD
NGC 4936	E2	59.6	-22.52	13.05	55.5	1.9	4.66	3.7	2.3	SD
NGC 5044	E0	52.2	-21.92	39.16	127.6	—	4.93	18.9	11.5	F
NGC 5077	S0	52.2	-21.38	16.29	53.1	0.7	4.64	12.0	5.6	RE
NGC 5090	E2	60.1	-21.92	3.97	17.1	—	4.33	1.7	1.2	SD
NGC 5102	S0	3.0	-17.38	51.49	0.5	—	2.65	1.0	0.3	SD
NGC 5419	S0	73.5	-22.89	4.14	26.7	—	4.34	4.4	2.9	SD
NGC 5532	S0	133.3	-22.85	6.02	128.0	—	5.02	12.6	10.2	F
NGC 5812	E0	40.7	-21.22	5.83	11.5	1.3	3.98	2.1	2.1	SD
NGC 5813	E1	34.9	-21.30	11.30	16.5	—	4.14	6.2	2.3	F
NGC 5831	E4	34.9	-20.41	2.29	3.4	1.8	3.44	1.2	0.4	SD
NGC 5846	S0	34.9	-21.81	28.02	40.9	—	4.45	5.8	4.1	RE
NGC 5864	SB0	33.9	-20.02	14.27	19.6	—	4.21	10.0	3.9	RE
NGC 5898	S0	44.3	-21.31	16.38	38.5	—	4.50	8.0	7.4	RE
NGC 5903	E3/S0	44.3	-21.49	5.21	12.2	—	4.00	5.3	3.5	RE
NGC 5920	S0	265.6	-22.75	< 0.20	< 13.8	—	—	—	—	—
NGC 6034	E?	205.1	-22.18	< 0.10	< 4.0	—	—	—	—	—
NGC 6305	E/S0	47.7	-20.81	< 0.16	< 0.5	—	—	—	—	—
NGC 6407	E	80.3	-22.09	< 0.06	< 0.5	1.2	—	—	—	—
NGC 6483	E	85.2	-22.02	< 0.06	< 0.5	1.4	—	—	—	—
NGC 6721	E1	76.7	-21.74	9.42	66.3	2.3	4.78	7.2	5.9	RE
NGC 6758	E2	58.8	-21.54	6.83	28.2	1.8	4.38	12.2	7.1	RE
NGC 6776	E1 pec	94.4	-22.16	6.93	73.8	1.0	4.63	8.0	4.7	F
NGC 6851	E4	48.6	-20.92	5.19	14.7	1.9	4.00	4.1	4.9	RE
NGC 6861	S0	48.6	-21.51	19.85	56.0	1.5	4.74	5.9	3.0	RE
NGC 6868	E3/S0	48.6	-21.94	27.65	78.0	1.2	4.71	7.8	4.2	RE
NGC 6875	S0	54.1	-20.89	2.59	9.1	—	3.84	5.0	3.5	RE
NGC 6876	E3	67.9	-22.33	< 0.27	< 1.5	—	—	—	—	—
NGC 6909	E5	48.6	-20.92	< 0.03	< 0.1	—	—	—	—	—
NGC 6936	S0	110.6	-21.70	7.67	92.8	—	4.88	15.0	4.6	F
NGC 6964	E pec	70.8	-20.87	2.57	12.7	—	4.02	2.8	1.3	SD
NGC 7014	E5	83.5	-21.59	13.25	110.5	1.1	4.96	14.7	11.7	RE
NGC 7029	S0	49.4	-21.05	2.17	6.3	—	3.72	3.7	3.5	SD
NGC 7041	S0/E7	32.8	-20.63	3.59	4.6	—	3.58	5.6	2.9	RE
NGC 7049	S0/Sa	38.1	-21.34	29.71	51.7	—	4.64	10.1	9.4	RE
NGC 7192	S0	48.6	-21.24	7.79	22.0	—	4.33	8.7	7.7	RE
NGC 7196	E3/S0	50.5	-21.17	3.39	10.3	—	3.93	5.5	4.2	RE
NGC 7562	E2	61.3	-21.57	1.64	7.4	2.3	3.78	3.7	2.9	SD
NGC 7619	E3	61.3	-22.01	6.09	27.4	2.1	4.35	2.8	1.3	SD
NGC 7626	E1	61.3	-21.88	< 0.20	< 0.9	—	—	—	—	—
NGC 7796	E1	56.4	-21.37	< 0.02	< 0.1	1.8	—	—	—	—
IC 1459	E	29.0	-21.48	37.93	38.1	—	4.35	5.6	5.5	RE
IC 4296	E0	65.0	-22.64	< 0.06	< 0.4	—	—	—	—	—
IC 4797	E pec	46.6	-21.49	< 0.29	< 0.8	—	—	—	—	—
IC 4889	S0	43.5	-21.28	9.48	21.4	—	4.13	7.6	5.7	RE
IC 5105	E5	93.5	-22.43	2.36	24.7	1.3	4.31	5.2	2.3	SD

Notes to the table:

Ionized gas morphologies are coded as follows:

SD: small disk; RE: regular extended; F: filamentary.

The line ratios $[\text{NII}]\lambda 6584/\text{H}\alpha$ have been taken from PJDSB, TdSA and GHJN; a constant value = 1.38 has been assumed for those objects with no spectroscopic information. M_{HII} is the computed mass of the ionized gas, in solar masses. D_{maj} and D_{min} are respectively the major and the minor diameter of the line-emitting region.

4. Results

4.1. Ionized gas morphology

A large fraction of E (72%) and S0 (85%) galaxies in our sample contain ionized gas; our rate of detection is larger than the results of previous imaging surveys (cf. $\sim 57\%$, GHJN), and spectroscopic surveys ($\sim 50\%$, PJDSB; $\sim 40\%$, Caldwell 1984). The $H\alpha + [NII]$ luminosities range between $10^{38} - 10^{41}$ erg s $^{-1}$.

The ionized gas morphology appears to be rather smooth for most galaxies; however a significant fraction ($\sim 12\%$ of the galaxies), show a very extended filamentary structure. According to the morphology and size of the line-emitting region, the galaxies were classified into three broad classes:

- 1) small disk (SD): in some cases with quite faint and short filaments; the mean diameter is $\lesssim 4$ kpc;
- 2) regular extended (RE): similar to the previous class, but larger in size (4 to 18 kpc), with short filaments sometimes present;
- 3) filaments (F): if a conspicuous filamentary structure dominates the morphology, often departing from a more regular disk-like inner region. It can extend as far as 10 kpc from the galaxy center.

For each galaxy in our sample with detected emission, Figs. 9 displays the $H\alpha + [NII]$ emission (left panel) and the R isophotes (right panel). North is up and East to the left for all images. For each object we give the lowest $H\alpha + [NII]$ contour level, which corresponds to the flux threshold level, in units of 10^{-16} erg s $^{-1}$ cm $^{-2}$ arcsec $^{-2}$, and the faintest R isophotes, in R -mag arcsec $^{-2}$. Contours are spaced 1 mag apart. Also, we give the resolution (FWHM) of each emission-line image. All emission-line images have been slightly smoothed by convolution with a gaussian of $\sigma = 1$ pixel.

The groups frequency distribution for our galaxies have been analyzed in order to correlate the gas morphology with the morphological type of the galaxy (E or S0; Fig. 3) and with its blue absolute magnitude M_B . Of all the S0 galaxies that show gas emission, 55% belong to the RE class, 34% to the SD class, and 11% to the filamentary class. The distribution for ellipticals is 25% for the RE, 54% for the SD, and 21% for the filamentary class. Therefore, elliptical galaxies that show SD gas structure are more frequent than those with RE structure, while it is the other way around for S0 galaxies. This is in line with the properties of stellar disks, which are both more luminous and larger in size in lenticular than in elliptical galaxies (see Scorza & Bender 1995). No apparent correlation is however found between the boxyness parameter a_4 and either the luminosity or the size of the $H\alpha + [NII]$ emission. A detailed analysis of the correlations between the morphology and the kinematics of the ionized-gas and that of the stellar component will be the subject of a forthcoming paper.

There is no clear correlation between the gas morphology and the galaxy luminosity. While galaxies with filamentary structure tend to be more luminous, both in the optical bands and in $H\alpha + [NII]$, and those with small disks are generally fainter, at any given optical luminosity there is a range of about 1 dex in the mean diameter of the emitting region. On the other hand, the tighter correlation between the $H\alpha + [NII]$ luminosity and the size of the emitting region suggests that the $H\alpha + [NII]$ luminosity is mainly related to the extension of the gas distribution rather than to its projected brightness.

4.2. Mass of ionized gas

The total ionized gas mass can be derived from the $H\alpha$ luminosities under the assumption of case B recombination (Osterbrock 1974). We have derived the pure $H\alpha$ luminosities using the $[NII] 6584/H\alpha$ line ratios published in PJDSB, TdSA and GHJN, or adopting a constant value $[NII] 6584/H\alpha = 1.38$, that is the average found by PJDSB for their spectroscopic set of early-type galaxies (the ratio $[NII] 6584/[NII] 6548$ is kept constant = 3.0, see PJDSB).

For a given electron temperature and density the mass can be written as:

$$M(HII) = (L_{H\alpha} m_H / N_e) / (4\pi j_{H\alpha} / N_e N_p) \quad (6)$$

where m_H is the mass of the hydrogen atom; N_e and N_p are the number of electrons and protons per cm $^{-3}$ and $j_{H\alpha}$ is the emission coefficient of $H\alpha$. Following PJDSB we have assumed an electron temperature of 10^4 K and an electron density of 10^3 e $^{-}$ cm $^{-3}$. The estimated masses are listed in Table 4. The mass values range between 10^3 and 10^5 solar masses, in broad agreement with those derived by GHJN. Because of the range of line ratios displayed by early-type galaxies (depending on total luminosity and other galaxian parameters), and of the possible deviation of the gas temperature and density from the assumed values, these masses should be considered only as rough estimates.

5. Correlations

There have been previous attempts at determining the relationship between the hot ($10^6 - 10^7$ K) X-ray emitting gas and the warm ($\sim 10^4$ K) $H\alpha$ -emitting gas. TdSA have found that on average galaxies with a larger content of hot gas also show a more powerful line emission; however, a large scatter in the relation indicates that other parameters must play a role.

The EINSTEIN sample of early-type galaxies (Fabbiano et al. 1992) have been analyzed statistically by Eskridge et al. (1995) to search for correlations between the X-ray luminosity and a variety of fundamental parameters of the galaxies. They found a significant correlation of the X-ray luminosities with the blue luminosities, the X-ray color index C_{12} , the magnesium index Mg_2 and the

central velocity dispersion σ_0 , in the sense that those systems with the deepest potential wells have the highest L_X and Mg_2 values. Also, L_X correlates with the axial ratio a/b : rounder galaxies tend to have higher L_X and L_X/L_B . Galaxies with high L_X are usually boxy (i.e. with a negative a_4 coefficient; Bender et al. 1989). The blue luminosity is found to correlate with a/b and the isophotal shape descriptor a_4 , but not with the IRAS luminosities in either the 12 μm and the 100 μm bands. They suggest that it is the potential well that appears to govern both the ability to retain the ISM at the present epoch and to retain the enriched ejecta of early star formation bursts.

We have analyzed the possible relationships between the warm and the hot gaseous components of the ISM of the galaxies in our sample through the statistical correlation between the total $L_{H\alpha}$ and L_X luminosities. The X-ray fluxes for the sample galaxies have been taken from the EINSTEIN database (as published in Fabbiano et al. 1992), complemented by data taken from ROSAT observations published in Brinkmann et al. (1994). A significant correlation, though with a quite large scatter, between $H\alpha+[NII]$ and X-ray luminosities is found for those galaxies (27% of the sample) for which we have detected ionized gas and are listed as X-ray sources (see Fig. 4).

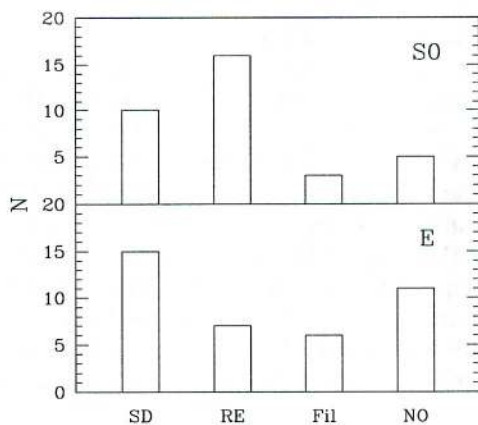


Fig. 3. Distribution of gas morphologies among ellipticals and among lenticulars. ‘NO’ means no detection

The strongest $L_{H\alpha+[NII]}$ galaxies also have strong L_X and present a more extended ionized gas distribution. However, among the remaining galaxies of the sample, there are relatively strong X-ray emitting galaxies for which we have not detected $H\alpha+[NII]$ emission (for instance NGC 6034 and IC 4296) and objects which show emission-lines but are not listed either in the EINSTEIN or the ROSAT databases (for example NGC 6868 and NGC 7014). Upper limits for $L_{H\alpha+[NII]}$ and L_X are indicated in the figures by arrows. The distribution of the datapoints in the diagram shows that, while there is a

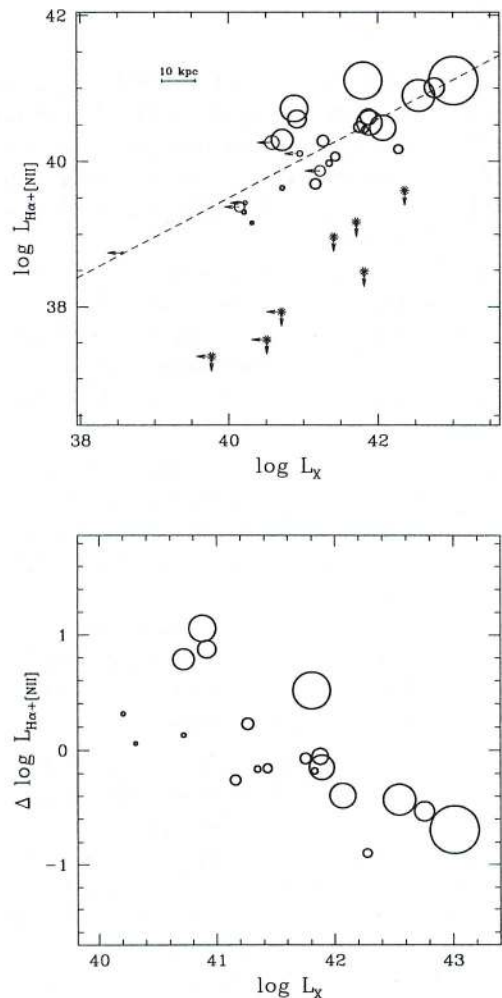


Fig. 4. *Upper panel:* $H\alpha+[NII]$ luminosities plotted against X-ray luminosities. The size of each point is proportional to the size (mean diameter, i.e. $\sqrt{D_{maj} \times D_{min}}$) of the line-emitting region. Upper limits are marked with arrows. A least square fit to the datapoints gives a slope of 0.54. *Lower panel:* Residuals of $L_{H\alpha+[NII]}$ with respect to the best fitting line with slope 1

number of galaxies with significant X-ray luminosity but undetected in $H\alpha+[NII]$, the location of the upper limits on L_X alone is consistent with the general correlation between L_X and $L_{H\alpha+[NII]}$ exhibited by the galaxies with measured values in both quantities. Taken at face value, this seems to suggest that the presence of hot gas is a condition necessary but not sufficient for the presence of warm gas.

The lower panel of Fig. 4 shows, for those galaxies with positive detections in both X-ray and $H\alpha+[NII]$ emissions, the residuals of $L_{H\alpha+[NII]}$ with respect to the values computed assuming a direct relation (slope = 1) between $L_{H\alpha+[NII]}$ and L_X . It is evident that galaxies with higher L_X values have a relatively lower amount of ionized gas.

The relationship between the warm gas and the far-infrared radiation produced by cold dust has been examined by comparing the $L_{\text{H}\alpha+\text{[NII]}}$ luminosities with L_{FIR} computed from the 60 and 100 μm bands; no correlation has been found. (Infrared fluxes have been taken from Knapp et al. 1989). TdSA found no correlation between the masses of dust derived from IRAS infrared observation and the $\text{H}\alpha+\text{[NII]}$ luminosities. Nevertheless the physical association of dust and ionized gas in elliptical galaxies has been shown to exist from deep optical CCD imaging by GHJN. Figure 5 shows a correlation between the infrared luminosity in the 12 μm band and $L_{\text{H}\alpha+\text{[NII]}}$. As in the correlation between $L_{\text{H}\alpha+\text{[NII]}}$ and L_X there seems to be galaxies with a significant $\text{H}\alpha+\text{[NII]}$ luminosity but with only upper limits on the 12 μm emission, and vice versa galaxies with significant infrared emission at this wavelength but little or no warm gas.

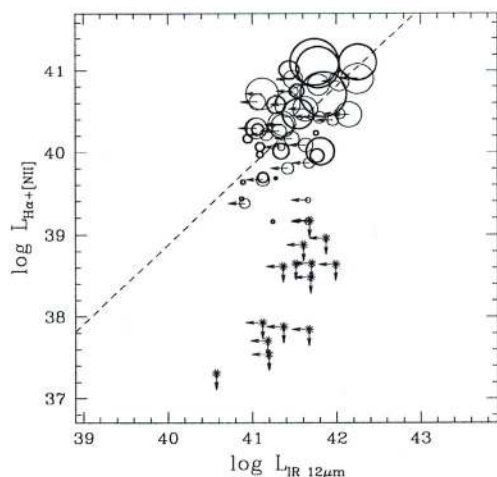


Fig. 5. $\text{H}\alpha+\text{[NII]}$ luminosities plotted against infrared luminosities in the 12 μm band. Symbols as in the previous figure. The slope of the least-square fit to the datapoints (dashed line) is 0.97

No significant correlations were found with radio integrated and core luminosities (from Wrobel 1991 and Wrobel & Heeschen 1991), although the intersection of our sample with the radio database is quite small and does not permit to draw any firm conclusion.

A weak correlation was found, for our galaxy sample, between $L_{\text{H}\alpha+\text{[NII]}}$ and the velocity dispersions σ_0 , taken from the compilation by McElroy (1995) (Fig. 6). These correlations are in the sense that those systems with the deepest potential wells have the highest $\text{H}\alpha+\text{[NII]}$ luminosities. A similar result was found between L_X and σ_0 . No correlation was found between $L_{\text{H}\alpha+\text{[NII]}}$ and Mg_2 for the present sample. We have also looked for evidence of correlation between $\text{H}\alpha+\text{[NII]}$ luminosities and the merger history as parameterized by the “fine structure” index de-

finied by Schweizer & Seitzer (1992), finding no correlation for the 9 galaxies in common with Schweizer and Seitzer’s sample.

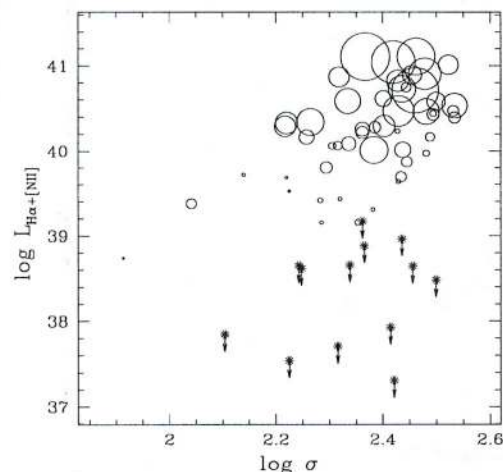


Fig. 6. Correlation between the central velocity dispersions and the $\text{H}\alpha+\text{[NII]}$ luminosities

Finally we have investigated the correlation between the $\text{H}\alpha+\text{[NII]}$ luminosities and the total blue luminosities of the galaxies (Fig. 7a). The weak trend present with total B luminosities becomes much more evident when $L_{\text{H}\alpha+\text{[NII]}}$ is plotted versus the blue luminosity inside the region occupied by the line-emitting gas, $L_B(<\text{emitt.})$ (Fig. 7b). We have defined $L_B(<\text{emitt.})$ as the total luminosity inside a centered circular region with diameter equal to the mean diameter of the line-emitting region. This same result is obtained using fluxes instead of luminosities, which supports the fact that this is a real correlation, and not an artifact of selection effects (faint emission in nearby galaxies would be easier to detect than in more luminous and distant galaxies).

6. Ionization mechanisms

There are several potential mechanisms that can account in part or fully for the observed gas ionization. Among the competing theories are photoionization by hot young stars (Kim 1989, S91), by hot old stars (di Serego Alighieri et al. 1990, BMSB) or radiation originating in an active nucleus, and/or shock ionization (Heckman et al. 1989). Conductive heating by electrons associated with the X-ray emitting coronal halo is another alternative proposed to explain the observed emission lines and their excitation character (SMG; Donahue & Voit 1991). In this section we will test the applicability of some of these hypotheses to our observations and results.

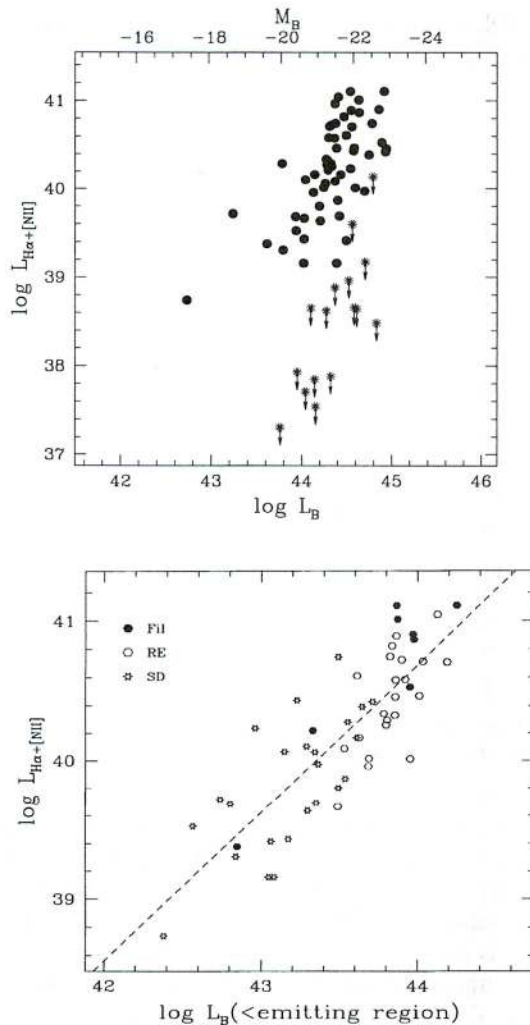


Fig. 7. The $H\alpha+[NII]$ luminosities are plotted against the total B luminosities (*upper panel*) and the B luminosities computed within the line-emitting region (*lower panel*). The slope of the least square fit (dashed line) is 1.06

6.1. Photoionization by post-AGB stars

The tight correlation between $L_{H\alpha+[NII]}$ and optical luminosity inside the emitting region strongly suggests a stellar origin for the ionizing photons. Recently BMSB have found that post-AGB stars provide sufficient ionizing radiation to account for the observed $H\alpha$ luminosities and equivalent widths in very early-type galaxies. Following the prescriptions by BMSB, we have calculated for our galaxies the predicted $H\alpha$ luminosities from stars in the post-AGB phase and compared them with the observed $H\alpha$ luminosities.

According to the recombination theory, case B (Osterbrock 1974), $7.34 \cdot 10^{11}$ Lyman continuum photons are necessary to produce 1 erg of $H\alpha$ luminosity. The total number of ionizing photons $Q(H)$ can be calculated assuming a specific photon luminosity of $7.3 \cdot 10^{40}$ quanta/s/ M_{\odot} ,

and multiplying by the total mass of stars (in solar units) inside the emitting region, M^* ; this in turn is derived from the blue luminosity L_B inside the emitting region, assuming an integrated stellar mass-to-light ratio $M/L_B = 8$ (BMSB).

Table 5 lists the blue luminosity, stellar masses, predicted number of ionizing photons, predicted $L_{H\alpha}$ and the ratio between the predicted and observed $H\alpha$ luminosities. We have found that for a large fraction of galaxies the ratios are of order unity, while several objects display values larger than 2, suggesting that the post-AGB stars provide a sufficient number of ionizing photons within the $H\alpha$ emitting region. The agreement with the four galaxies in common with BMSB (NGC 4636, NGC 5846, NGC 6868 and IC 1459) is fair, considering the different gas luminosities and extensions we have found compared to their data. The presence of predicted/computed $H\alpha$ luminosity ratios significantly larger than 1 is not an embarrassment, as there are several alternatives to explain an excess of available and unused photons. First, the covering factor of the gas can be below unity, as it is likely for ellipticals, which typically are not gas rich systems. In these cases, a significant fraction of extreme ultraviolet photons will escape to the intergalactic space, instead of being reprocessed by the interstellar medium. Post-AGB stars exist wherever there is an old stellar population, but it is not necessarily so for the gas, which, as observed, has a more complex and irregular distribution than the stellar component.

Another possible explanation is that some of the emitting clouds are not visible due to the large opacity of the dust along the line of sight. The galaxies in our sample have extensive dust systems, which are closely associated, at least morphologically, with the emission line gas. (We are currently completing the analysis of the dust characteristics, which will be the subject of a second paper in this series). It is possible that in the cases where there is significant amount of dust we calculate the correct value of $Q(H)$ from the blue luminosity, but we underestimate the $H\alpha$ luminosity.

6.2. Thermal conduction

Conductive heating of the warm gas by hot electrons associated with an X-ray emitting coronal halo typically found within elliptical galaxies offers an alternative excitation mechanism, as proposed by Sparks & Collier-Cameron (1988) and SMG. In this scenario, each galaxy has an associated pre-existing coronal halo, that is a diffuse hot gaseous plasma which pervades the galaxy. We then suppose that the galaxy accretes cold gas and dust either in a minor merger or as a result of a tidal encounter with a gas-rich companion. The process of thermal electron conduction then causes energy to flow from the hot coronal component into the cold gas which simultaneously excites the cold gas into emission while locally cooling the

Table 5. Derived data on ionized gas

Ident.	$\log L_B(\text{emitt})$	$\log M_*$	$\log N_{\text{ph}}$	$\log L_{\text{H}\alpha}$	$L_{\text{H}\alpha \text{ calc}}/L_{\text{H}\alpha \text{ obs}}$
NGC 524	43.95	11.27	52.13	39.56	5.16
NGC 533	43.97	11.29	52.15	40.45	0.69
NGC 584	43.80	11.12	51.98	39.81	2.05
NGC 636	42.80	10.12	50.99	39.23	0.78
NGC 720	43.56	10.88	51.74	39.83	1.11
NGC 741	43.76	11.08	51.94	40.01	1.47
NGC 1172	42.85	10.17	51.03	38.92	1.75
NGC 1399	43.61	10.93	51.79	39.71	1.65
NGC 1407	43.35	10.67	51.53	39.24	2.67
NGC 1453	44.19	11.51	52.37	40.26	1.78
NGC 1600	43.95	11.27	52.14	40.08	1.56
NGC 3268	43.08	10.40	51.27	38.79	4.06
NGC 3311	43.06	10.38	51.25	38.96	2.63
NGC 3379	43.17	10.49	51.35	38.98	3.24
NGC 3489	42.74	10.06	50.92	39.26	0.62
NGC 3607	42.84	10.16	51.02	38.85	2.00
NGC 4105	43.81	11.13	51.99	39.84	1.92
NGC 4472	43.36	10.68	51.55	39.52	1.45
NGC 4473	43.05	10.37	51.23	38.70	4.58
NGC 4486	43.98	11.30	52.16	40.56	0.43
NGC 4552	43.30	10.62	51.48	39.20	2.60
NGC 4636	43.15	10.47	51.33	39.62	0.71
NGC 4936	43.50	10.82	51.68	40.29	0.33
NGC 5044	43.86	11.18	52.05	40.56	0.42
NGC 5077	43.90	11.22	52.08	40.27	0.88
NGC 5090	42.96	10.28	51.14	39.96	0.21
NGC 5102	42.38	9.70	50.56	38.28	2.59
NGC 5419	43.71	11.03	51.90	39.97	1.14
NGC 5532	44.25	11.57	52.43	40.65	0.82
NGC 5812	43.34	10.66	51.53	39.61	1.12
NGC 5813	43.41	10.73	51.59	39.78	0.74
NGC 5831	42.56	9.88	50.75	39.07	0.65
NGC 5846	43.54	10.86	51.72	40.08	0.71
NGC 5898	43.92	11.24	52.10	40.13	1.28
NGC 5903	43.53	10.85	51.71	39.63	1.64
NGC 6721	43.84	11.16	52.02	40.42	0.55
NGC 6758	44.01	11.33	52.19	40.01	2.07
NGC 6776	43.97	11.29	52.16	40.26	1.08
NGC 6851	43.63	10.95	51.81	39.63	2.07
NGC 6861	43.84	11.16	52.02	40.38	0.59
NGC 6868	43.87	11.19	52.05	40.34	0.70
NGC 6875	43.69	11.01	51.87	39.47	3.38
NGC 6964	43.37	10.69	51.55	39.65	0.90
NGC 7014	44.13	11.45	52.31	40.59	0.71
NGC 7029	43.50	10.82	51.68	39.35	2.92
NGC 7041	43.49	10.81	51.67	39.21	3.94
NGC 7049	44.03	11.36	52.22	40.27	1.21
NGC 7192	43.78	11.11	51.97	39.96	1.39
NGC 7196	43.69	11.01	51.87	39.56	2.80
NGC 7562	43.54	10.86	51.72	39.41	2.77
NGC 7619	43.23	10.55	51.41	39.98	0.36
IC 1459	43.86	11.18	52.04	39.98	1.56
IC 4889	43.85	11.18	52.04	39.76	2.60
IC 5105	43.64	10.96	51.83	39.94	1.05

Notes to the table:

$\log L_B(< \text{emitt.})$ is the B -band luminosity inside the line-emitting region; $\log M_*$ is the corresponding stellar mass (assuming $M/L = 8$); $\log N_{\text{ph}}$ is the number of ionizing photons; $\log L_{\text{H}\alpha}$ is the “pure” $\text{H}\alpha$ luminosity, computed from $L_{\text{H}\alpha + [\text{NII}]}$ and the line ratio $[\text{NII}]\lambda 6584/\text{H}\alpha$. The last column gives the ratio between the predicted and the computed $\text{H}\alpha$ luminosity.

coronal gas. The energy radiated by the cold gas (the optical emission filament system in this picture) is simply the heat flux into the filaments. Quantitatively, this idea has worked well with previously studied objects and explains the dustiness of the gas as well as the X-ray spectral parameters (Sparks 1992). Here, we investigate whether such a mechanism is at all viable as a *general* excitation process for emission line gas in ellipticals.

Under the assumption that the available energy flux is in the saturated regime (Cowie & McKee 1977), the amount of energy available to excite the optical emission filaments is, following SMG, $Q_{\text{sat}} = 5.2 \cdot 10^{40} T_7^{3/2} n_{0.01} D_{\text{maj}} D_{\text{min}}$, where $T_7 = T/10^7$ is the temperature of the coronal halo and $n_{0.01} = n_e/0.01$ is its density. In terms of the observed emission line flux, that is

$$L_{\text{H}\alpha + [\text{NII}]} (\text{predicted}) = 1.5 \cdot 10^{39} T_7^{3/2} n_{0.01} D_{\text{maj}} D_{\text{min}} \quad (7)$$

assuming that $\sim 1\%$ of the available energy is radiated in the $\text{H}\alpha + [\text{NII}]$ lines and that the total surface area of the system is three times the apparent projected surface area.

The average coronal gas temperature for elliptical galaxies found by Kim et al. (1992) is $T \approx 1.5$ keV, while characteristic densities for the coronal gas in elliptical galaxies are $n_e \approx 0.01 \text{ cm}^{-3}$. With these values for the temperature and density, we predict a filament luminosity and show the comparison to observations in Fig. 8.

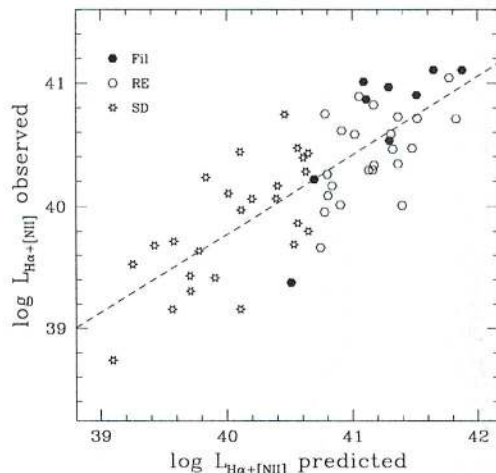


Fig. 8. The observed $\text{H}\alpha + [\text{NII}]$ luminosity is plotted versus the luminosity predicted according to the simple model of conductive heating of the warm gas by hot electrons emitted from the X-ray halo. The slope of least square fit (dashed line) is 0.64, the rms is 0.33

No account has yet been taken of the variation of coronal gas parameters such as temperature and density with galaxy size or mass, nor has any adjustment made to the

absolute normalization of SMG. The degree of correlation and the *absolute level* of the correlation are excellent, and demonstrate that an interpretation based on mergers and thermal interaction of hot and cold plasma components at this stage is perfectly consistent with the data.

7. Summary

We have shown the results of an optical imaging survey of 73 luminous early-type galaxies directed to study the properties of their interstellar medium. The galaxies were selected to span the entire variety of morphological types and isophotal shapes from E0 through S0/Sa, to provide a fair interval of optical luminosity, to include both radio-loud and radio-quiet, X-ray emitters and non-emitters

From our observations, which consisted of broad-band R and narrow-band images centered at the $\text{H}\alpha$ and $[\text{NII}]$ emission lines, we have derived and mapped the luminosity and morphological distribution of the ionized gas. We have found that a large fraction of E(72%) and S0(85%) galaxies in our sample contain measurable amounts of ionized gas. This high rate of detection and the measured integrated $\text{H}\alpha + [\text{NII}]$ fluxes are larger than those derived by previous studies. This is due, to a great extent, to the longer exposures, higher signal-to-noise ratio and therefore lower limiting fluxes in our sample when compared to other studies. This is apparent when direct comparison are made of the extended, faint filamentary structures seen in our data and those of previous studies.

When comparing the properties of the ionized gas with the morphological type of the galaxy, we find that the ellipticals have twice as many instances of extended filamentary structures (21%) than the S0 galaxies, but more than half (64%) of the ellipticals have emission concentrated in small disks. This is in line with the properties of stellar disks which are both more luminous and larger in size in lenticular than in elliptical galaxies. While there is at best a weak correlation between the extent of the filamentary structure and the overall galaxy luminosity, we find a tighter correlation between the $\text{H}\alpha + [\text{NII}]$ luminosity and the size of the emitting region. This indicates that the $\text{H}\alpha + [\text{NII}]$ luminosity is mainly related to the gas extension rather than to its projected brightness.

We have estimated the total mass of ionized gas for each galaxy, assuming that the case B recombination conditions are applicable, and an electron temperature of 10^4 K and density of $10 \text{ e}^- \text{ cm}^{-3}$. With these obviously rough assumptions, we derive total masses for the ionized gas in the range of $10^3 - 10^5 M_\odot$, well in line with previous results. To improve the accuracy of these results, as well as to derive kinematical information on the most interesting emission-line objects, we are carrying-out a program of long-slit spectroscopy, whose outcome will be the subject of a future publication.

We have explored the possible correlation between the hot ($10^6 - 10^7$ K) X-ray emitting gas and the warm (10^4 K)

H α -emitting component. For those galaxies in our sample which are both X-ray emitters and show the presence of ionized gas, we find a significant correlation between the X-ray and H α + [NII] luminosities. However among the remaining galaxies of the sample there are relatively strong X-ray emitters for which we have not detected H α + [NII] emission, and vice versa H α + [NII] emitters that are not listed in the catalogs of X-ray sources. The distribution of upper limits in the $L_{\text{H}\alpha+\text{[NII]}}-L_X$ diagram suggests that warm gas is only found in galaxies with a substantial amount of hot gas, while the presence of hot gas does not necessarily imply that of the warm component.

We have estimated the emission-line flux under the assumption that the excitation mechanism is conductive heating of the warm gas by hot electrons associated with an X-ray emitting coronal halo. The predicted H α + [NII] luminosity correlates extremely well with the measured values. We must note however that this correlation holds even for those galaxies where there is no measured X-ray emission, and therefore it cannot be construed as a proof that X-ray conduction by hot electrons is necessarily the only mechanism responsible for the observed line-emission.

This has an important bearing on our understanding of the mechanisms responsible for the heating and ionization of the hot and warm gas, and whether we should invoke a single mechanism, and therefore expect strong a correlation between the two gas phases, or seek separate but somehow related mechanisms, and therefore expect weaker correlations. This issue is still very much open and will require further observations, as well as additional theoretical work.

A reasonable correlation was found between the H α + [NII] luminosities and the infrared IRAS 12 μm luminosities, but no correlation was found with the 60 μm and 100 μm luminosities.

We found weak correlation between the H α + [NII] luminosity and the velocity dispersion of the galaxy, in the sense that those systems with the deepest potential wells have the highest emission-line luminosities. On the other hand, there is a strong correlation between the blue-luminosities within the emitting region and the emission-line luminosity. This is an important result which shows that the source of the ionizing photons is distributed in the same way as the stellar population.

A mechanism with the necessary characteristics is that proposed by BMSB, who found that post-AGB stars provide sufficient ionizing radiation to account for the observed H α luminosities and equivalent widths in early-type galaxies. For our galaxies, we have calculated the predicted H α luminosities produced by stars in the post-AGB phase and compared them with the observed H α luminosities. We find that in all cases the ratios are of the order of unity or greater, meaning that the post-AGB stars can produce all the necessary ionizing photons and

are distributed as required to effectively produce the H α fluxes. In several cases there is even a remarkable excess of ionizing photons, which are then probably lost to the galaxy because of covering factors less than unity. The post-AGB stars are therefore a very plausible and attractive ionization mechanism to explain the observed H α luminosity. We know that they do exist, are distributed in the same way as the rest of the old stellar population in the galaxy and therefore can account naturally for several of the observed correlations (eg. with the blue luminosity, with the size of the emitting region, with the velocity dispersion, etc.). However, the observed correlation with the X-ray fluxes cannot be directly explained by the presence of post-AGB stars, and a different mechanism must be invoked. More extensive observations, in particular long-slit spectroscopy, as well as more work on the theoretical modeling of the mechanisms responsible for the X-ray flux, are clearly needed.

Acknowledgements. These observations were obtained at the ESO telescopes in La Silla, within the ESO Key-Programme 1-004-43K. We thank the ESO staff for their support. N. Caon acknowledges the receipt of an ESA Fellowship. M. Pastoriza acknowledges the support and hospitality of the STScI during a sabbatical visit. We dedicate this paper to the memory of our good friend and colleague, Jean-Luc Nieto, who was one of the leaders in the field of early-type galaxies and a member of our Key-Programme team.

References

- Bender R., Surma P., Döbereiner S., Möllenhoff C., Madejsky R., 1989, *A&A* 217, 35
- Binette L., Magris C.G., Stasińska G., Bruzual A.G., 1994, *A&A* 292, 13 (=BMSB)
- Brinkmann W., Siebert J., Boller Th., 1994, *A&A* 281, 355
- Buson L.M., Sadler E.M., Zeilinger W.W., et al., 1993, *A&A* 280, 409
- Caldwell N., 1984, *PASP* 96, 287
- Cowie L.L., McKee C.F., 1977, *ApJ* 211, 135
- Davies R.L., Burstein D., Dressler A., et al., 1987, *ApJS* 64, 581
- de Vaucouleurs A., Longo G., 1987, *The Univ. of Texas Monographs in Astron.*, 5
- de Vaucouleurs G., de Vaucouleurs A., Corwin H.G. Jr., et al., 1991, *Third Reference Catalogue of Bright Galaxies*. Springer-Verlag, New York
- di Serego Alighieri S., Trinchieri G., Brocato E. 1990, in: Fabbiano G., Gallagher J.S., Renzini A. (eds.), *Windows on Galaxies*. Kluwer, Dordrecht, p. 301
- Donahue M., Voit G.M., 1991, *ApJ* 381, 361
- Eschridge P.B., Fabbiano G., Kim D.-W., 1995, *ApJ* 442, 523
- Fabbiano G., Kim D.-W., Trinchieri G., 1992, *ApJS* 80, 531
- Fabian A.C., 1994, *ARAA* 32, 277
- Fosbury R.A.E., Bokserberg A., Snijders M.A.J., et al., 1982, *MNRAS* 201, 991
- Goudfrooij P., Hansen L., Jørgensen H.E., Nørgaard-Nielsen H.U., 1994, *A&AS* 105, 341 (=GHJN)

- Hansen L., Jørgensen H.E., Nørgaard-Nielsen H.U., 1991, *A&A* 243, 49
- Heckman T., Baum S.A., vanBreugel W.J.M., McCarthy P., 1989, *ApJ* 338, 48
- Jerjen H., Tammann G., 1993, *A&A* 276, 1
- Kim D.-W., 1989, *ApJ* 346, 653
- Kim D.-W., Fabbiano G., Trinchieri G., 1992, *ApJ* 393, 134
- Knapp G.R., Guhathakurta P., Kim D.-W., Jura M., 1989, *ApJS* 70, 387
- Kraan-Korteweg R.C., 1986, *A&AS* 66, 255
- Macchetto F., Sparks W.B., 1992, in: Busarello G., Capaccioli M., Longo G. (eds.), *Morphological and Physical Classification of Galaxies*. Kluwer, Dordrecht, p. 191
- McElroy D., 1995, *ApJS* 100, 105
- McMillan R., Ciardullo R., Jacoby G.H., 1994, *AJ* 108, 1610
- Osterbrock D.E., 1974, *Astrophysics of Gaseous Nebulae*. W.H. Freeman & Co., San Francisco
- Phillips M.M., Jenkins C.R., Dopita M.A., Sadler E.M., Binette L., 1986, *AJ* 91, 1062 (=PJDSB)
- Poulain P., Nieto J.-L., 1994, *A&AS* 103, 573
- Sadler E.M., Gerhard O.E., 1985, *MNRAS* 214, 177
- Sandage A.R., Tammann G., 1987, (a revised) *Shapley-Ames Catalog of Bright Galaxies* (2nd ed.). Carnegie, Washington
- Schweizer F., Seitzer P., 1992, *AJ* 104, 1039
- Scorza C., Bender R., 1995, *A&A* 293, 20
- Shields J., 1991, *AJ* 102, 1314 (=S91)
- Singh K.P., Bhat P.N., Prabhu T.P., Kembhavi A.K., 1995, *A&A* 302, 658
- Sparks W.B., 1992, *ApJ* 399, 66
- Sparks W.B., Collier-Cameron A., 1988, *MNRAS* 232, 215
- Sparks W.B., Macchetto F., Golombek D., 1989, *ApJ* 345, 153 (=SMG)
- Sparks W.B., Wall J.V., Thorne D.J., et al., 1985, *MNRAS* 217, 87
- Trinchieri G., di Serego Alighieri S., 1991, *AJ* 101, 1647 (=TdSA)
- Wrobel J.M., 1991, *AJ* 101, 127
- Wrobel J.M., Heeschen D.S., 1991, *AJ* 101, 148

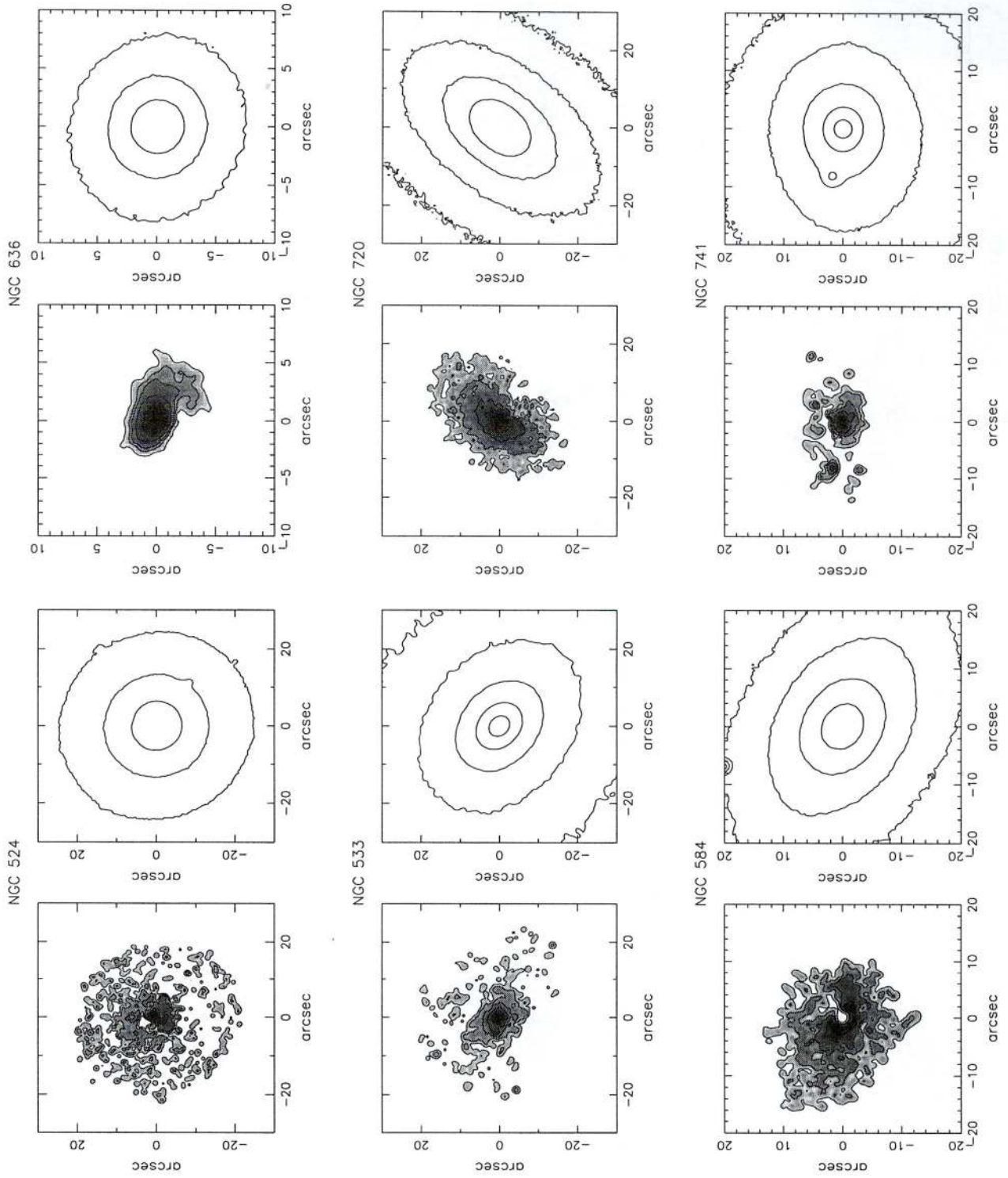


Fig. 9. NGC 524. $H\alpha$ + [NII]: 0.2; R : 22.0; FWHM= $1''.4$; NGC 533. $H\alpha$ + [NII]: 0.3; R : 22.0; FWHM= $1''.5$; NGC 584. $H\alpha$ + [NII]: 0.5; R : 20.0; FWHM= $1''.3$; NGC 636. $H\alpha$ + [NII]: 0.7; R : 19.0; FWHM= $1''.7$; NGC 720. $H\alpha$ + [NII]: 0.8; R : 21.0; FWHM= $1''.6$; NGC 741. $H\alpha$ + [NII]: 0.3; R : 21.0; FWHM= $1''.4$

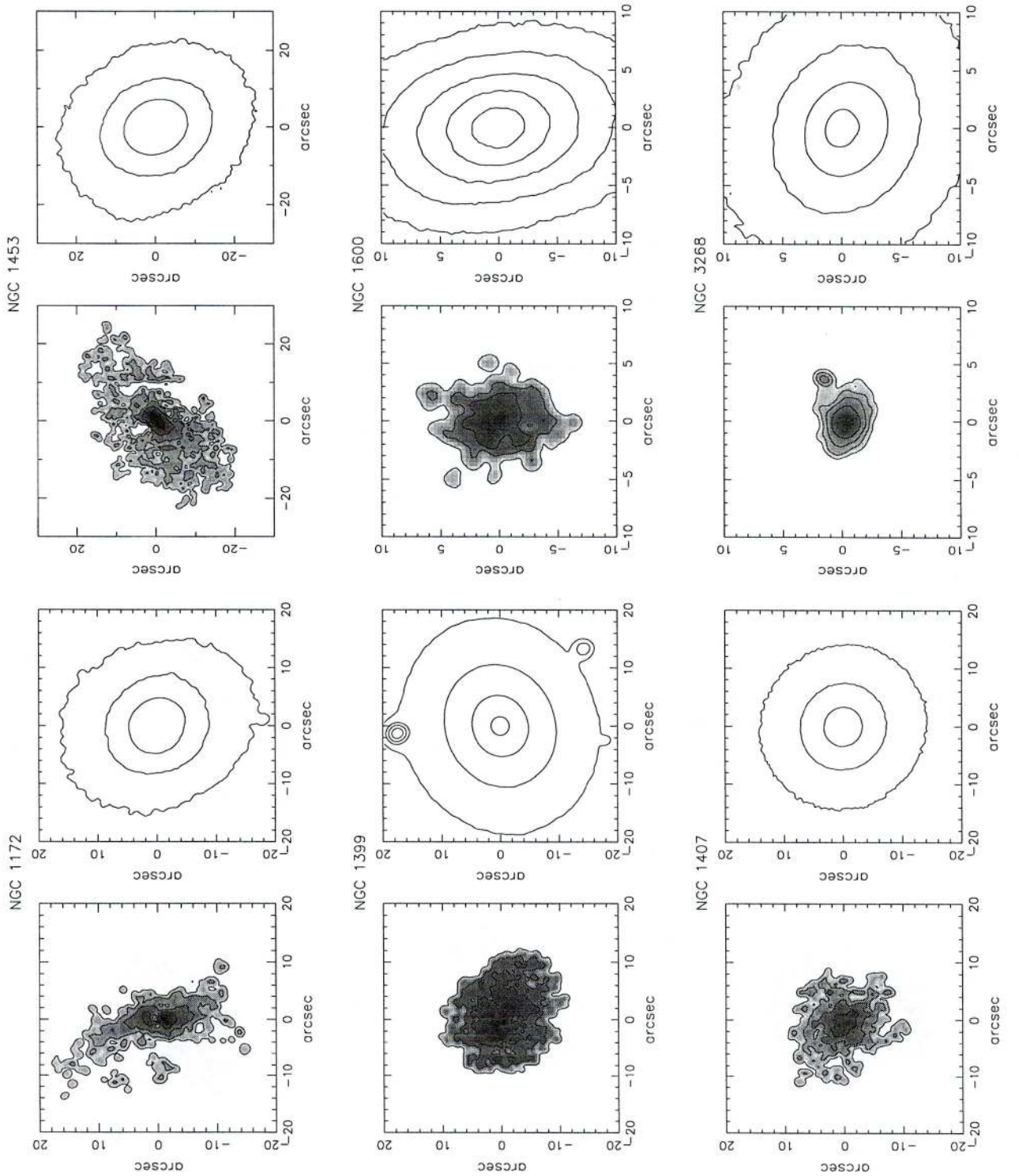


Fig. 9. NGC 1172. $H\alpha$ + [NII]: 0.25; R : 21.0; FWHM= $1''.2$; NGC 1399. $H\alpha$ + [NII]: 1.0; R : 19.0; FWHM= $1''.4$; NGC 1407. $H\alpha$ + [NII]: 0.4; R : 19.0; FWHM= $1''.3$; NGC 1453. $H\alpha$ + [NII]: 0.2; R : 21.0; FWHM= $1''.7$; NGC 1600. $H\alpha$ + [NII]: 0.5; R : 19.5 (step= 0.5 mag); FWHM= $1''.3$; NGC 3268. $H\alpha$ + [NII]: 0.1; R : 20.0; FWHM= $1''.1$

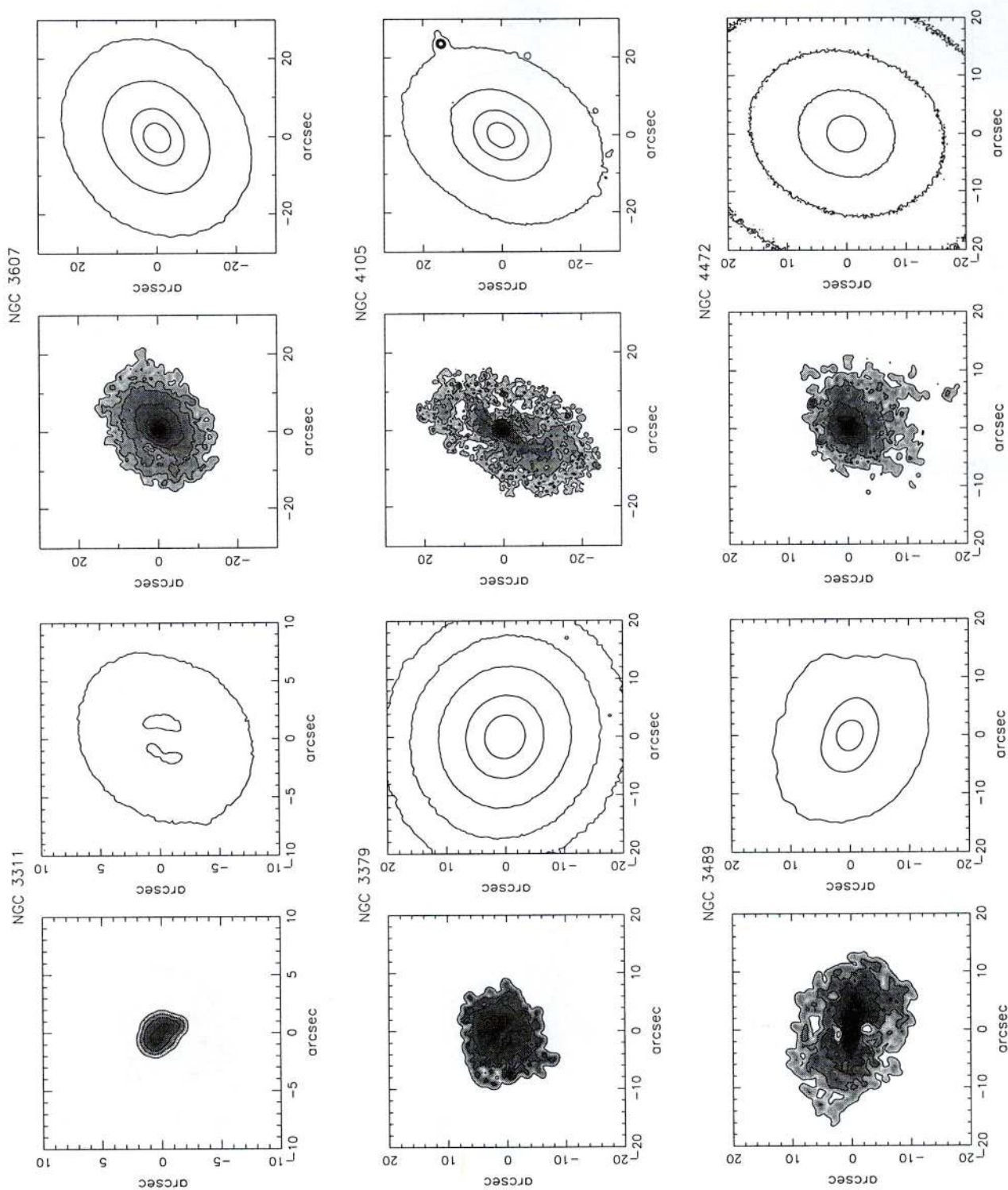


Fig. 9. NGC 3311. $H\alpha$ + [NII]: 0.6; R : 21.0; FWHM= $1''.2$; NGC 3379. $H\alpha$ + [NII]: 0.6; R : 20.0; FWHM= $1''.1$; NGC 3489. $H\alpha$ + [NII]: 1.7; R : 18.0; FWHM= $1''.6$; NGC 3607. $H\alpha$ + [NII]: 0.3; R : 20.0; FWHM= $2''.1$; NGC 4105. $H\alpha$ + [NII]: 0.4; R : 20.0; FWHM= $0''.8$; NGC 4472. $H\alpha$ + [NII]: 1.5; R : 19.0; FWHM= $1''.0$

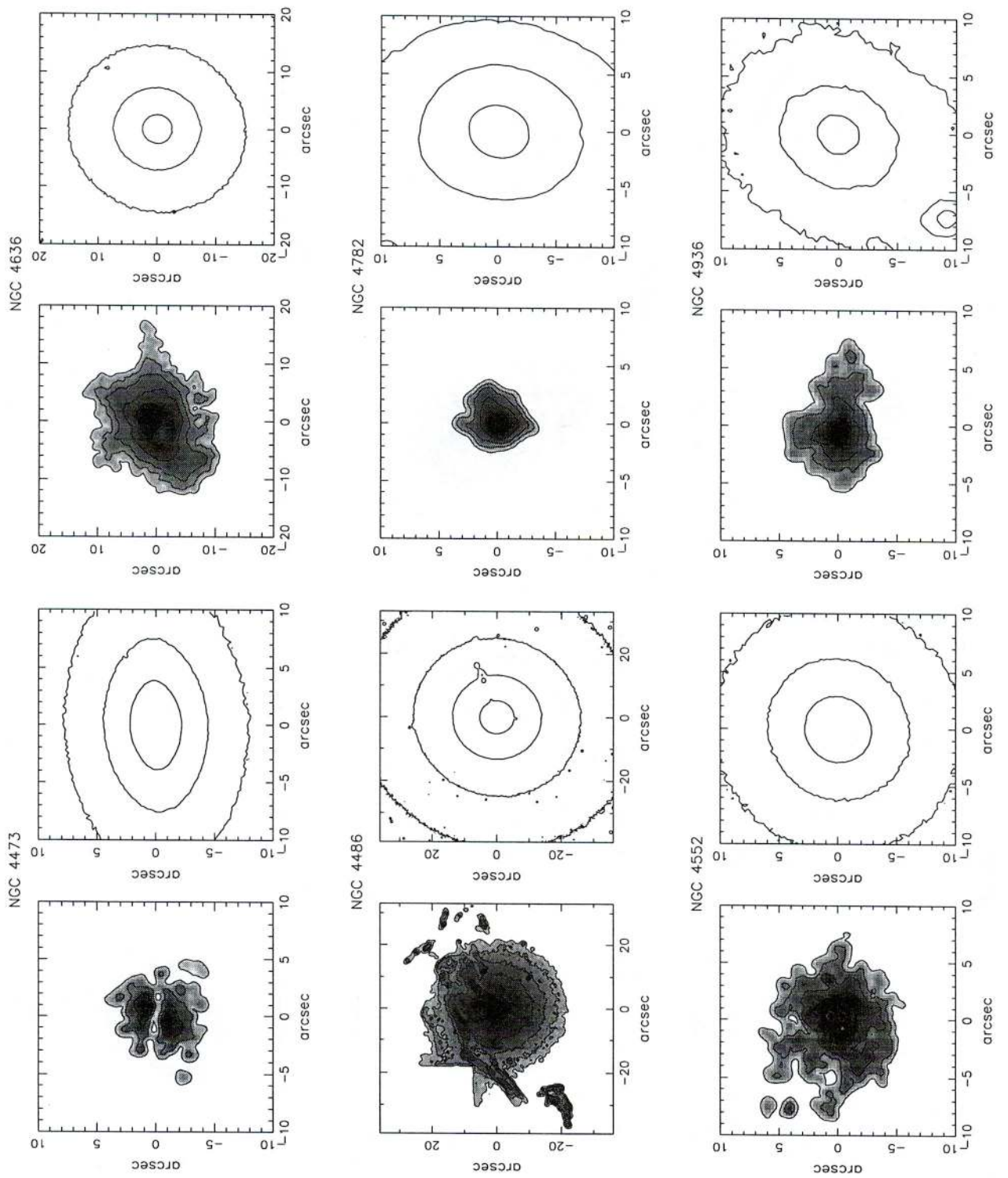


Fig. 9. NGC 4473. $H\alpha+[NII]$: 1.5; R : 18.0; FWHM= $1''.0$; NGC 4486. $H\alpha+[NII]$: 0.5; R : 22.0; FWHM= $0''.8$; NGC 4552. $H\alpha+[NII]$: 1.0; R : 18.0; FWHM= $1''.1$; NGC 4636. $H\alpha+[NII]$: 0.4; R : 19.0; FWHM= $1''.8$; NGC 4782. $H\alpha+[NII]$: 0.7; R : 19.0; FWHM= $1''.2$; NGC 4936. $H\alpha+[NII]$: 2.1; R : 19.0; FWHM= $1''.0$

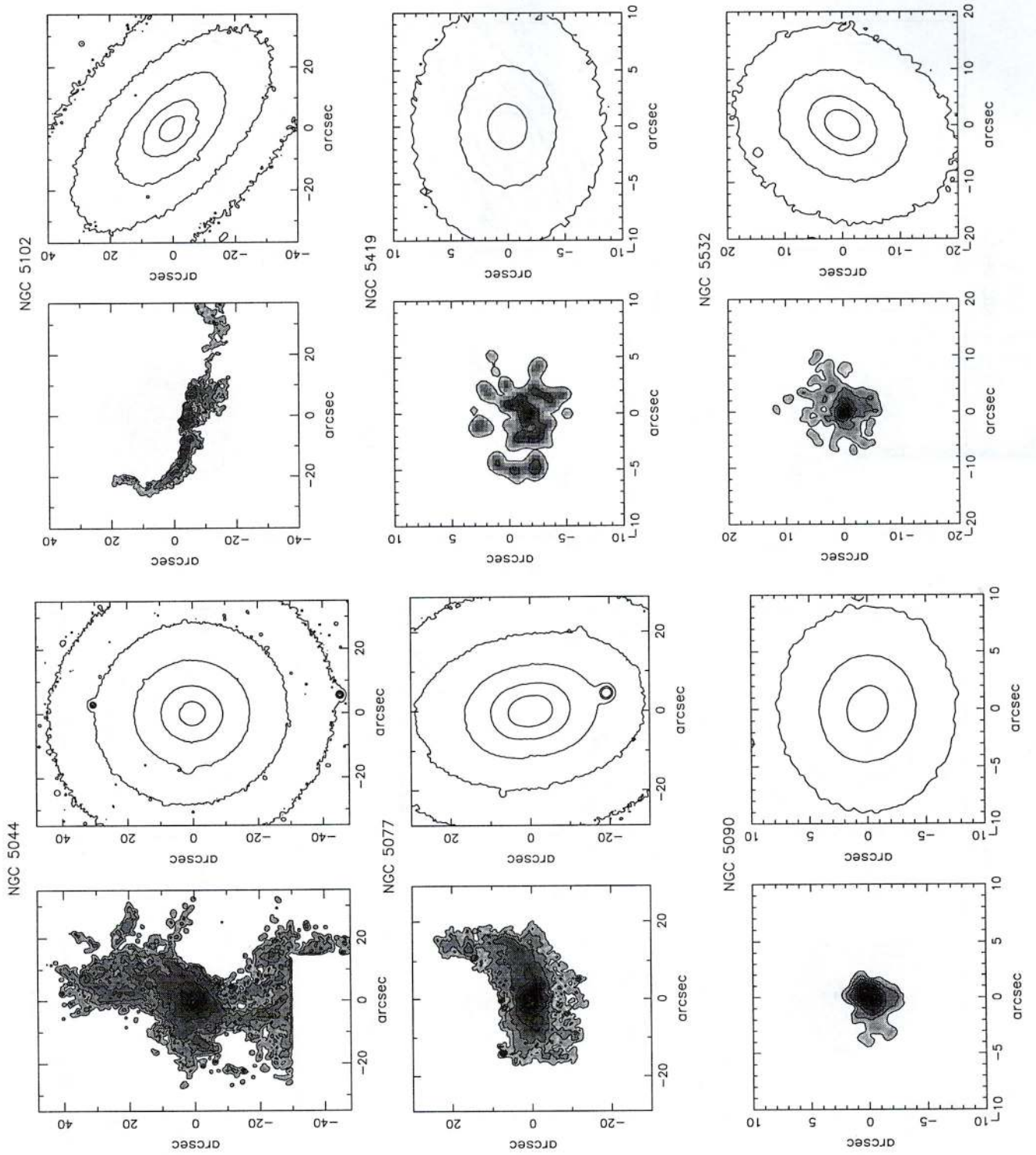


Fig. 9. NGC 5044. H α + [NII]: 0.1; R : 22.0; FWHM= 1".0. The removal of a ghost image mutilated the H α + [NII] emission map in the lower part of the plot. NGC 5077. H α + [NII]: 0.25; R : 22.0; FWHM= 1".1; NGC 5090. H α + [NII]: 1.1; R : 19.0; FWHM= 0".9; NGC 5102. H α + [NII]: 1.2; R : 21.0; FWHM= 0".9; NGC 5419. H α + [NII]: 4.0; R : 19.0; FWHM= 1".3; NGC 5532. H α + [NII]: 0.9; R : 21.0; FWHM= 1".2

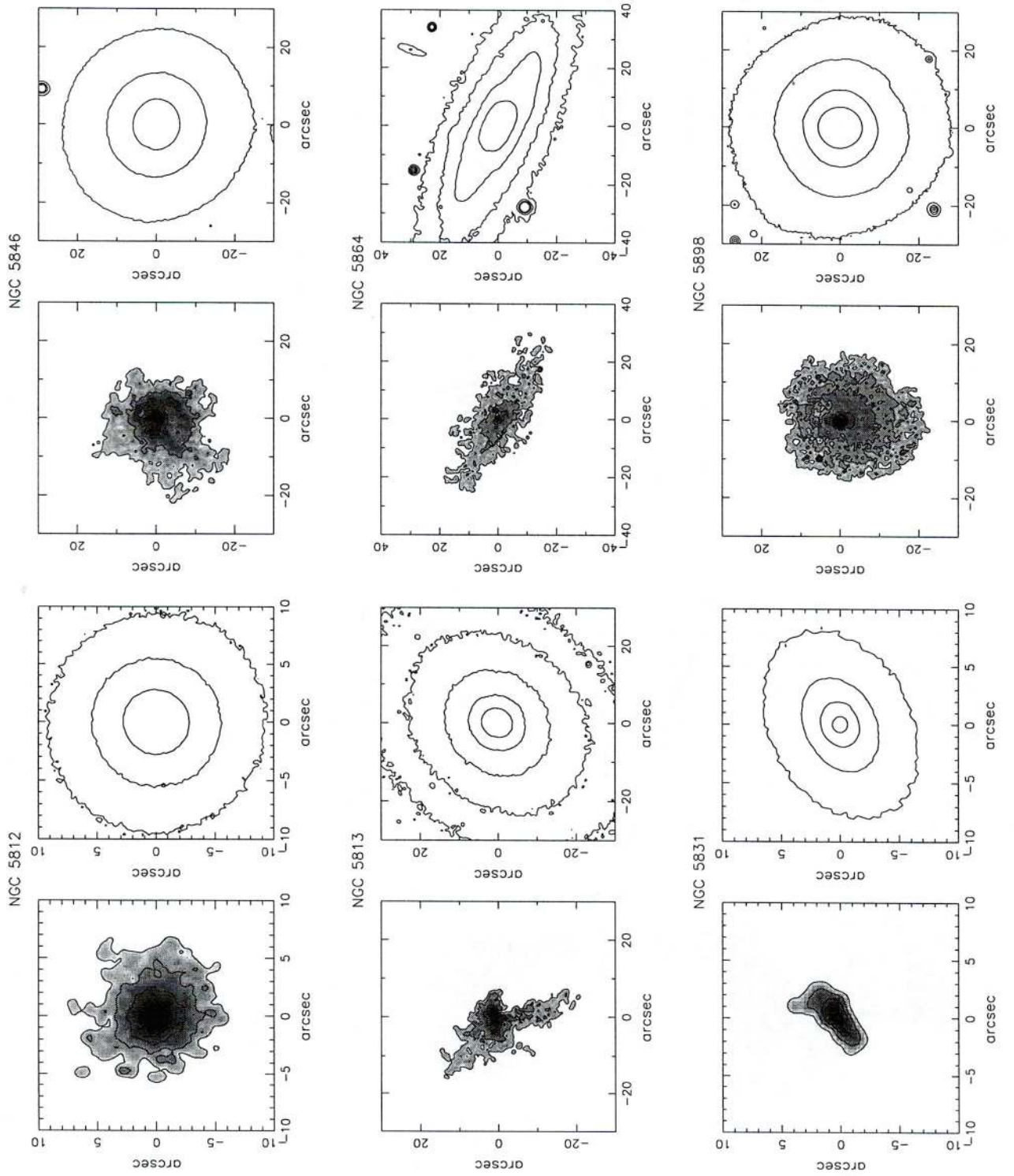


Fig. 9. NGC 5812. H α + [NII]: 1.2; R : 18.0; FWHM= 1''1; NGC 5813. H α + [NII]: 1.2; R : 22.0; FWHM= 1''0; NGC 5831. H α + [NII]: 6.6; R : 19.0; FWHM= 1''2; NGC 5846. H α + [NII]: 1.5; R : 21.0; FWHM= 1''1; NGC 5864. H α + [NII]: 1.0; R : 22.0; FWHM= 1''5; NGC 5898. H α + [NII]: 0.3; R : 21.0; FWHM= 1''0

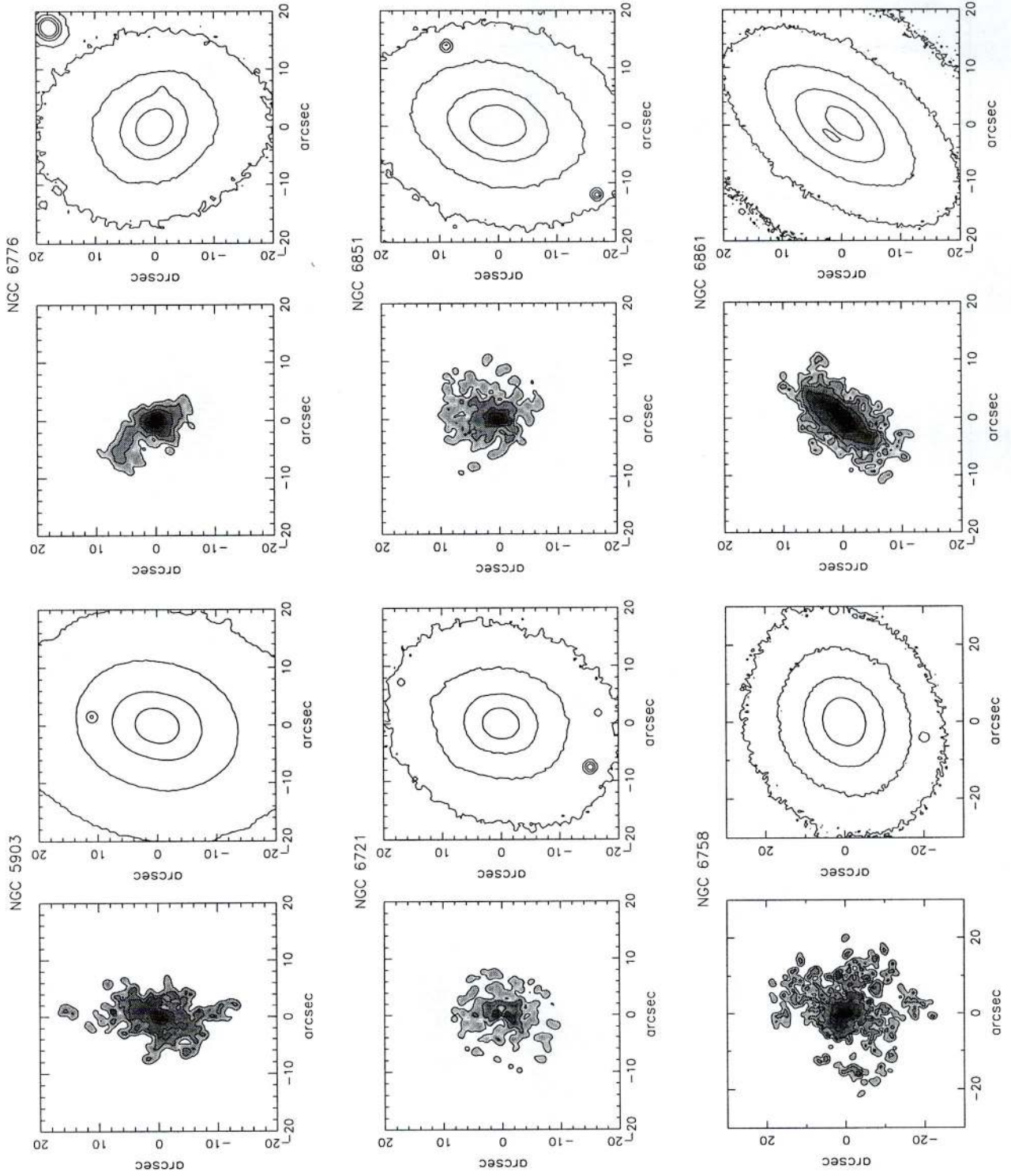


Fig. 9. NGC 5903. $H\alpha+[NII]$: 0.5; R : 20.0; FWHM= $1''.2$; NGC 6721. $H\alpha+[NII]$: 3.4; R : 21.0; FWHM= $1''.0$; NGC 6758. $H\alpha+[NII]$: 0.2; R : 22.0; FWHM= $1''.6$; NGC 6776. $H\alpha+[NII]$: 1.1; R : 21.0; FWHM= $1''.3$; NGC 6851. $H\alpha+[NII]$: 0.9; R : 21.0; FWHM= $0''.9$; NGC 6861. $H\alpha+[NII]$: 0.4; R : 21.0; FWHM= $1''.0$

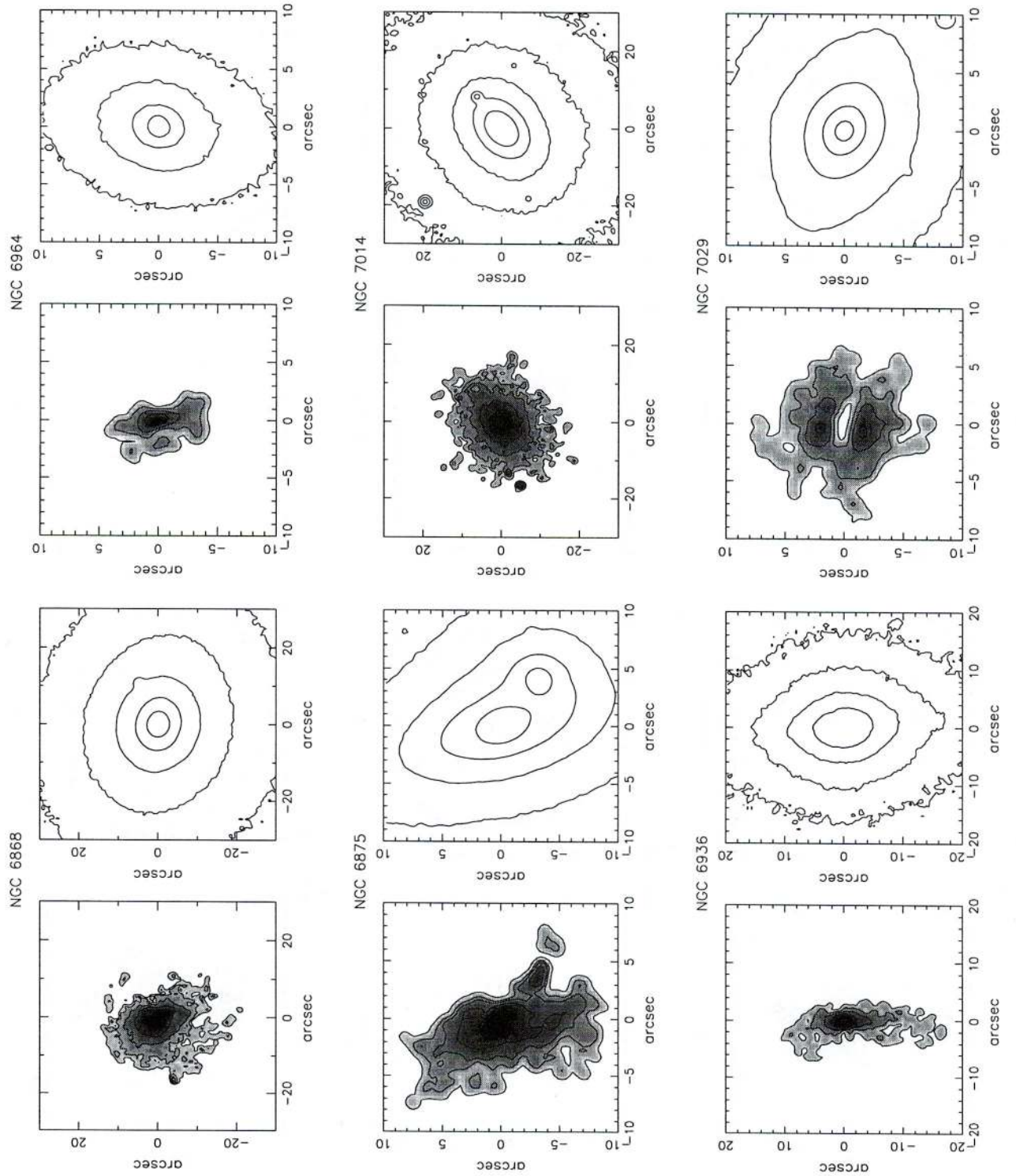


Fig. 9. NGC 6868. H α + [NII]: 0.5; R : 21.0; FWHM= 1''5; NGC 6875. H α + [NII]: 0.2; R : 20.0; FWHM= 0''9; NGC 6936. H α + [NII]: 1.0; R : 22.0; FWHM= 1''0; NGC 6964. H α + [NII]: 1.7; R : 20.0; FWHM= 1''0; NGC 7014. H α + [NII]: 0.2; R : 23.0; FWHM= 1''4; NGC 7029. H α + [NII]: 0.5; R : 20.0; FWHM= 1''4

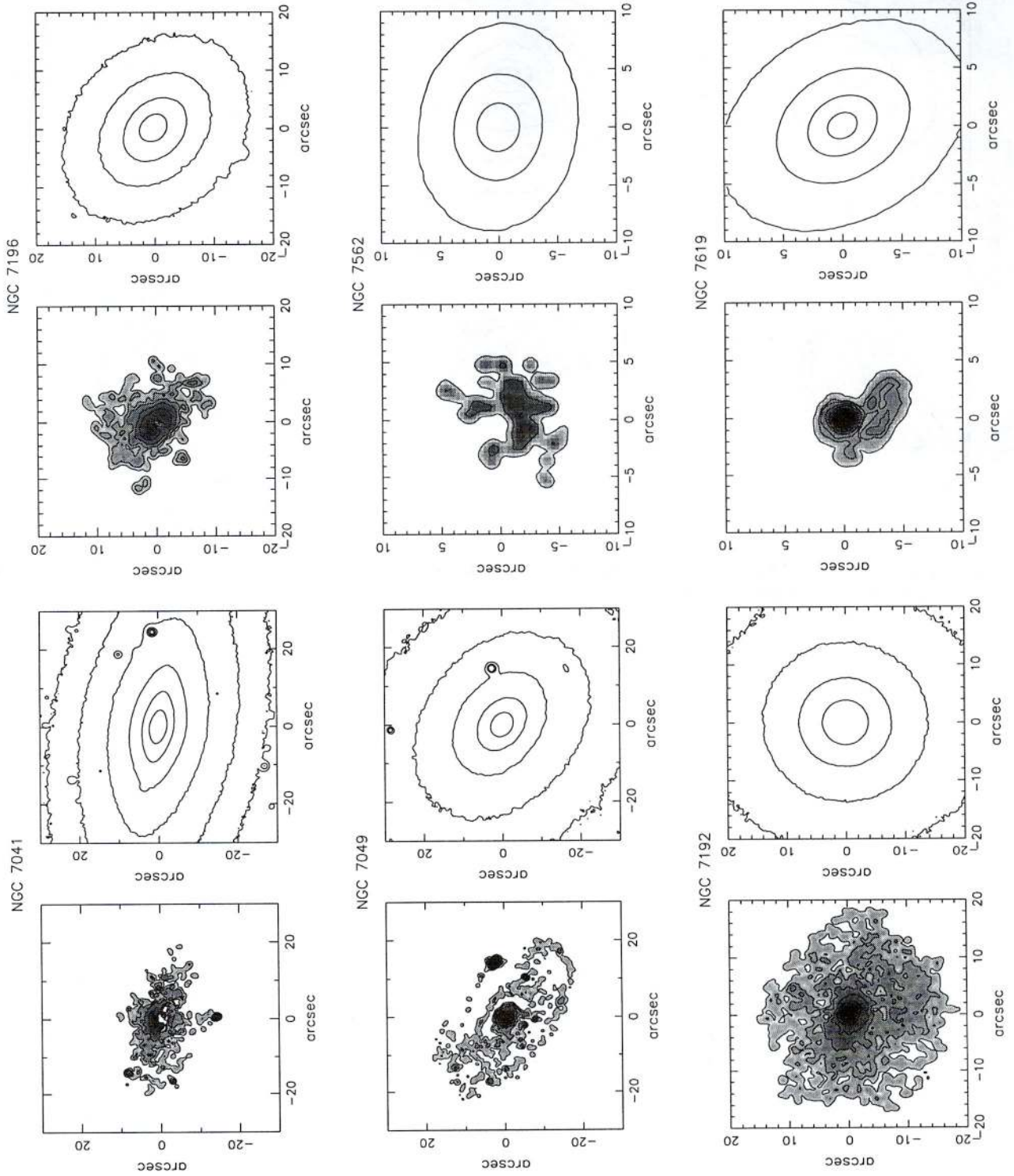


Fig. 9. NGC 7041. $H\alpha+[NII]$: 0.3; R : 22.0; FWHM = $1''.1$; NGC 7049. $H\alpha+[NII]$: 0.8; R : 21.0; FWHM = $1''.0$; NGC 7192. $H\alpha+[NII]$: 0.2; R : 21.0; FWHM = $1''.8$; NGC 7196. $H\alpha+[NII]$: 0.15; R : 21.0; FWHM = $1''.2$; NGC 7562. $H\alpha+[NII]$: 1.3; R : 19.0; FWHM = $1''.4$; NGC 7619. $H\alpha+[NII]$: 0.5; R : 19.0; FWHM = $1''.1$

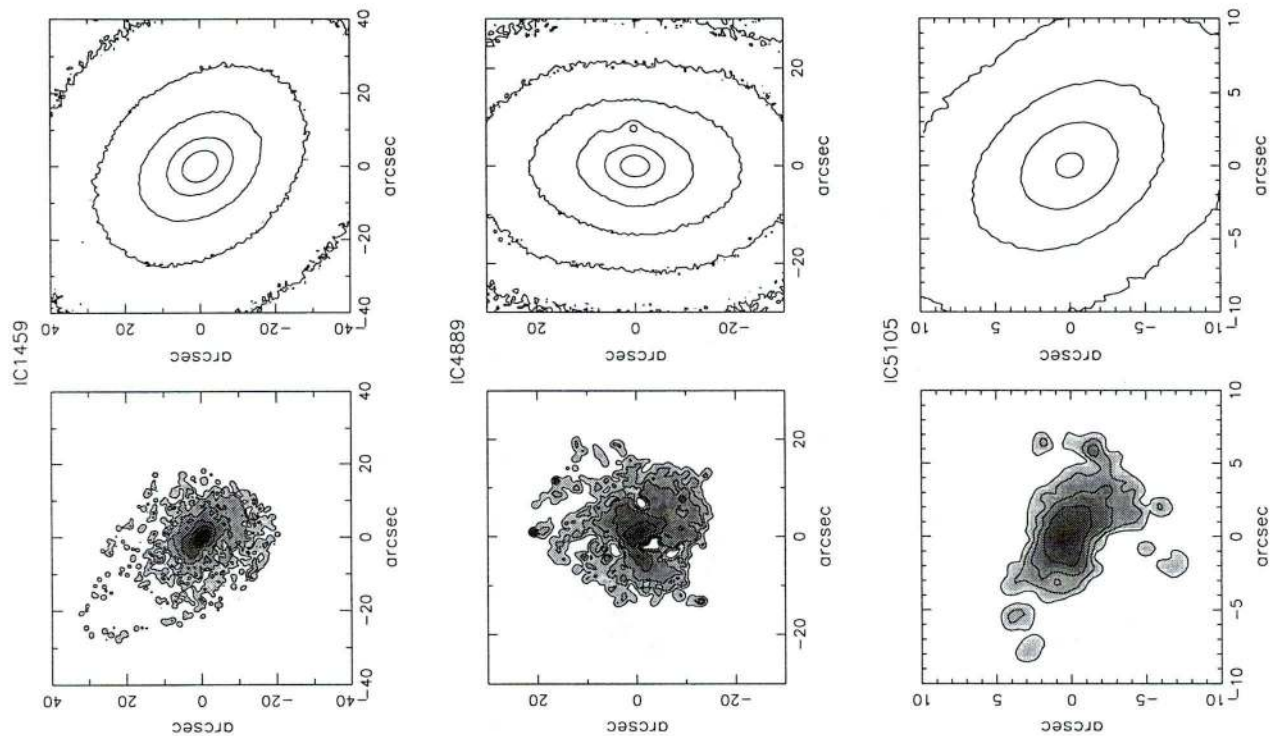


Fig. 9. IC 1459. $H\alpha$ + [NII]: 0.7; R : 21.0; FWHM= $0''.9$; IC 4889. $H\alpha$ + [NII]: 0.15; R : 22.0; FWHM= $1''.7$; IC 5105. $H\alpha$ + [NII]: 0.4; R : 20.0; FWHM= $1''.8$